

The IPSI Bgd Transactions on Internet Research

Multi-, Inter-, and Trans-disciplinary Issues in Computer Science and Engineering

A publication of

IPSI Bgd Internet Research Society
New York, Frankfurt, Tokyo, Belgrade
January 2011 Volume 7 Number 2 (ISSN 1820-4503)

Guest Editor: Nenad Filipović

Table of Contents:

| | |
|--|----|
| Low Reynolds Number flow in an Expanding Alveolated Duct Henry, F.; and Tsuda, A..... | 2 |
| Mining Data from Hemodynamic Simulations for Human Aorta Tošović, M.; Radović, M.; Petrović, D; Milašinović, D; Devedžić, G; Ranković, V; and Filipović, N. | 6 |
| A Back Spine Position Measuring System based on Accelerometer Data Peulic, A.; Högl, H.; Filipovic, N.; and Zoran, E..... | 11 |
| The Investigation of Flow – Structural Interaction in an Arterial Branching by Numerical Simulation Alin D.; Alexandru M.; and Mihaela M..... | 17 |
| Computer Simulation of Plaque formation and Development Filipovic, N.; Meunier, N.; Kojic, M.; Isailovic, V.; Radovic, M.; Milosevic, Z.; Nikolic, D.; Milasinovic, D.; Exarchos, T.; Parodi, O.; and Fotiadis, D..... | 22 |
| ARTool: A Platform for the Development of Multi-level patient-specific artery and atherogenesis models Exarchos, T.; Stefanou, K.; Siogkas, P.; Sakelarios, A.; Fotiadis, D.; Naka, K.; Michalis, L.; Filipovic, N.; Parodi, O..... | 29 |

The IPSI BgD Internet Research Society

The Internet Research Society is an association of people with professional interest in the field of the Internet. All members will receive this TRANSACTIONS upon payment of the annual Society membership fee of €100 plus an annual subscription fee of €1000 (air mail printed matters delivery).

Member copies of Transactions are for personal use only
IPSI BGD TRANSACTIONS ON ADVANCED RESEARCH

www.internetjournals.net

| STAFF | | |
|--|--|---|
| Veljko Milutinovic, Editor-in-Chief | Marko Novakovic, Journal Manager | |
| Department of Computer Engineering IPSI BgD Internet Research Society University of Belgrade POB 35-54 Belgrade, Serbia Tel: (381) 64-1389281 | Department of Computer Engineering IPSI BgD Internet Research Society University of Belgrade POB 35-54 Belgrade, Serbia Tel: (381) 64-2956756 | |
| vm@eff.rs | ipsi.journals@gmail.com | |
| EDITORIAL BOARD | | |
| Lipkovski, Aleksandar | Gonzalez, Victor | Victor Milligan, Charles |
| The Faculty of Mathematics, Belgrade, Serbia | University of Oviedo, Gijon, Spain | Sun Microsystems, Colorado USA |
| Blaisten-Barojas Estela | Janicic Predrag | Kovacevic, Milos |
| George Mason University, Fairfax, Virginia USA | The Faculty of Mathematics, Belgrade Serbia | School of Civil Engineering, Belgrade Serbia |
| Crisp, Bob | Jutla, Dawn | Neuhold, Erich |
| University of Arkansas, Fayetteville, Arkansas USA | Sant Marry's University, Halifax Canada | Research Studios Austria, Vienna Austria |
| Domenici, Andrea | Karabeg, Dino | Piccardi, Massimo |
| University of Pisa, Pisa Italy | Oslo University, Oslo Norway | Sydney University of Technology, Sydney Australia |
| Flynn, Michael | Kiong, Tan Kok | Radenkovic, Bozidar |
| Stanford University, Palo Alto, California USA | National University of Singapore Singapore | Faculty of Organizational Sciences, Belgrade Serbia |
| Fujii, Hironori | Kovacevic, Branko | Rutledge, Chip |
| Fujii Labs, M.I.T., Tokyo Japan | School of Electrical Engineering, Belgrade Serbia | Purdue Discovery Park, Indiana USA |
| Ganascia, Jean-Luc | Patricelli, Frederic | Mester, Gyula |
| Paris University, Paris France | ICTEK Worldwide L'Aquila Italy | University of Szeged, Szeged Hungary |

Low Reynolds Number flow in an Expanding Alveolated Duct

Henry, S., Frank; and Tsuda, Akira

Abstract—A numerical model of an expanding asymmetric alveolated duct was used to examine the influence of various features of acinar geometry on the structure of the flow and the transport of fluid particles in a typical alveolus in selected generations of the human acinus. We confirmed that the alveolar geometry affects the nature of the flow in alveoli, particularly in the proximal region of the acinus.

1. INTRODUCTION

WHILE slow viscous flow occurs in a number of biological situations, this paper is primarily concerned with gas and fluid particle transport in the human pulmonary acinus. The acinar region is defined to start at the transitional bronchioles; i.e., in the airways in which alveoli first appear. The Reynolds number ($Re = Ud/\nu$, where ν is the kinematic viscosity) of the flow in the acinar-entrance airways is of order one and thus inertial effects are relatively unimportant. The change in the flow rate over the breathing period is slow in comparison to the diffusional time; hence, acinar flow is quasi steady [1]. Nonetheless, the motion of the walls confining the flow is a defining feature of the flow. While in certain restricted circumstances a rigid model gives a reasonable description of alveolar flow, we will see that, in general, wall motion is central to the nature of alveolar flow.

In this paper, we use a numerical model [1] to examine the influence of various features of acinar geometry on the structure of the flow in a typical alveolus in selected generations of a typical human acinus. We have shown in the past [2,3] that the nature of the flow in an alveolus is governed largely by the value of QA/QD , where QA is the rate of flow entering the expanding alveolus and QD is that passing by the alveolar opening in the duct. We have also shown, using rigid models [4], that alveolar flow is influenced by the alveolus aspect ratio $AR = h/w$, where h is the depth and w the width, and the ratio of alveolar depth to duct diameter, $DR = h/d$. In an expanding model, both AR and DR are related to QA/QD and in this paper, we explore the effect of this relationship on the resulting alveolar flow patterns.

2. METHODS

2.1 Model Geometry

The model comprises three identical annular alveoli in axial alignment (Fig. 1a). Each alveolus has a width w , an outer diameter c , a septa of thickness t and an inner diameter d . The model geometry changes in a perfectly kinematically reversible, simple sinusoidal, manner. That is, all lengths change as $L(t) = \bar{L}F(t)$, where $F(t) = 1 + K \sin nt$, $K = (\phi - 1)/(\phi + 1)$, $\phi = (1 + C)^{1/3}$, $C = V_T/V_{FRC}$, $n = 2\pi/T$, V_T is the tidal volume, V_{FRC} is the lung volume at functional residual capacity, T is the breathing period and the over bar signifies the mean value. For quiet breathing, $T = 4s$ and $C = 0.2$ [5].

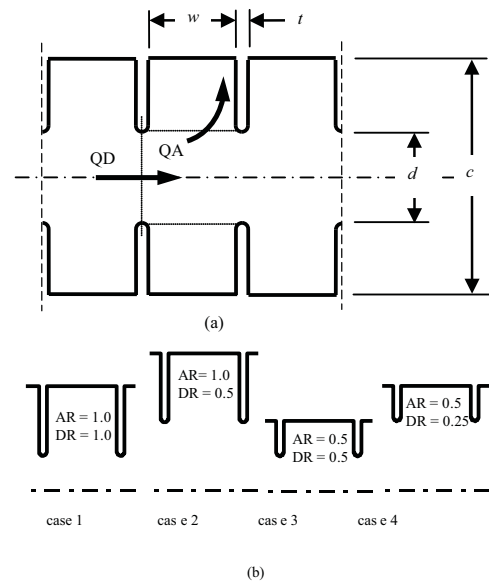


Figure 1: (a) Three-alveoli model. QA is the volume flow into the alveoli and QD is the volume flow in the duct. (b) Schematics of the four geometric configurations considered.

2.2 Flow and Geometrical Characteristics

The flow parameters we consider are the ratio of flow entering the alveolus to that passing by the alveolar opening in the duct, QA/QD (Fig. 1a) and the Reynolds number of the flow in the duct, Re . The geometric parameters are the alveolar aspect ratio, $AR = h/w$, where $h = (c - d)/2$; and the ratio of the depth to the inner duct

diameters, $DR = h/d$ (Fig. 1a). We concentrate on four geometric configurations (Fig 1b and Table 1). Specifically, case 1 has $AR = 1$ and $DR = 1$; case 2, $AR = 1$ and $DR = 0.5$; case 3, $AR = 0.5$ and $DR = 0.5$; and case 4, $AR = 0.5$ and $DR = 0.25$. Cases 1 and 2 are models of mature, fully-developed, alveoli; whereas, cases 3 and 4 are models of infant, developing, alveoli.

Table 1: Geometry and flow details

| Case | AR | DR | gen. | QA/QD | Re |
|------|-----|------|-------|-----------------------|--------|
| 1 | 1.0 | 1.0 | rigid | 0 | 1.0 |
| | | | 15 | 7.33×10^{-4} | 1.0 |
| | | | 18 | 7.22×10^{-3} | 0.1 |
| | | | 23 | 0.29 | 0.0025 |
| 2 | 1.0 | 0.5 | rigid | 0 | 1.0 |
| | | | 15 | 5.50×10^{-4} | 1.0 |
| | | | 18 | 5.43×10^{-3} | 0.1 |
| | | | 23 | 0.23 | 0.0024 |
| 3 | 0.5 | 0.5 | rigid | 0 | 1.0 |
| | | | 15 | 2.75×10^{-4} | 1.0 |
| | | | 18 | 2.73×10^{-3} | 0.1 |
| | | | 23 | 0.24 | 0.0011 |
| 4 | 0.5 | 0.25 | rigid | 0 | 1.0 |
| | | | 15 | 2.29×10^{-4} | 1.0 |
| | | | 18 | 2.27×10^{-3} | 0.1 |
| | | | 23 | 0.18 | 0.0013 |

As we have assumed that the geometry remains similar at all times, QA/QD is simply a function of model geometry. Specifically, $QA/QD = VA/VD$, where VA is the volume of the alveolus and VD is the total acinar volume distal of the alveolus plus VA and the duct volume below VA (Fig. 1). The value of VD defines in which generation the alveolus is located. We note that Re and QA/QD are linked through VD. In particular, we define $Re = U_{\max} \bar{d}/\nu$, where, U_{\max} is the maximum bulk velocity, and hence, $Re = 6K\bar{V}_D/\nu T\bar{d}$. We see that the Reynolds number is a function of the tidal volume, V_T (through K), and the breathing frequency, $1/T$.

2.3 Governing Equations

The Navier-Stokes equations, in cylindrical coordinates, were transformed into an equation for the transport of vorticity. An equation for the streamfunction was derived from the continuity equation. The vorticity and streamfunction equations were discretized on a moving mesh using the finite volume method. The resulting equations were solved on a multi-block grid using the line-by-line Gauss-Seidel method with implicit time marching. More details on the numerical solution and validation of the model are given in Henry & Tsuda (2010).

3. RESULTS

The instantaneous streamline patterns for the flow in the entrance-region alveoli did not change appreciably over the breathing period (Fig. 2). This confirms the finding of Tsuda et al., 1995,

that acinar flow is quasi steady. This was found to be true of all geometrical cases and generational locations considered (results not shown).

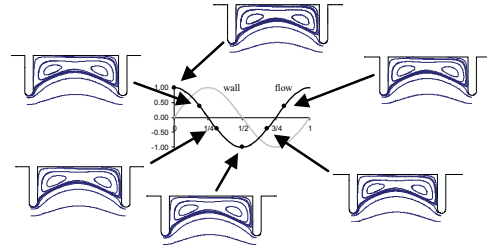


Figure 2: Instantaneous streamlines in generation 15 of geometry case 4 ($AR = 0.5$, $DR = 0.25$) at various points in the breathing cycle. See Table 1 for flow details.

In all cases, the predicted flow patterns in the entrance-region alveoli of the expanding models resemble those of the corresponding rigid cases (Figs 3-4). Nonetheless, the expanding model flows differ from the rigid cases in essence. Unlike the expanding cases, the flows in the rigid models have streamlines separating the duct flow from the alveolar flow and no streamlines emanate from the walls. It is noted that the further the alveolus is away from the acinar entrance, the more dissimilar are the expanding model streamline patterns from those of the rigid case. Specifically, in the terminal generation of all cases considered, the flow in the alveolus is largely radial (Figs. 3-4).

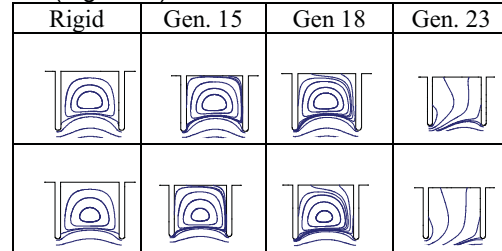


Figure 3: Instantaneous streamlines at maximum inhalation flow rate. Upper row, geometry case 1 ($AR = 1.0$, $DR = 1.0$). Lower row, geometry case 2 ($AR = 1.0$, $DR = 0.5$). See Table 1 for flow details.

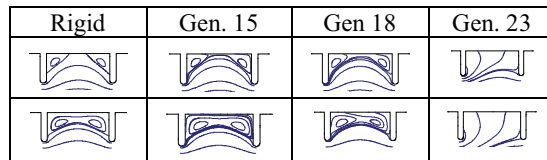


Figure 4: Instantaneous streamlines at maximum inhalation flow rate. Upper row, geometry case 3 ($AR = 0.5$, $DR = 0.5$). Lower row, geometry case 4 ($AR = 0.5$, $DR = 0.25$). See Table 1 for flow details.

The alveolar flow in geometry case 1 ($AR = 1$ and $DR = 1$) is quite similar to that in case 2 ($AR = 1$ and $DR = 0.5$) for all generations (Fig. 3). That is, the flow in fully developed alveoli does not appear to be affected by the alveolar depth to duct diameter ratio, DR. Conversely, the flows in the shallow, immature, alveoli, geometry cases 3 and 4, with $AR = 0.5$ (Fig. 4) differ considerably from one another in all generations considered

but the last. The sensitivity of the flow in the alveoli with $AR = 0.5$ to the value of DR was shown previously by Karl et al. (2004) in a rigid model. That is, when the inner diameter, d , is relatively small compared to the alveolus depth (large DR), the flow expands further into the alveolus than when d is relative large, (small DR). The result is that in case 3, two separate recirculation regions occur; whereas, in the case 4, two recirculation zones also appear but they are encircled by a larger closed streamline (Fig 4).

The expanding model flows differ from the rigid cases in another important way. As shown by Tsuda et al. (1995), when expanding cavity flows exhibit closed streamlines, a stagnation saddle point must exist near the wall. Here we find that when there are two regions with closed streamlines, as in the case 3 ($AR = 0.5$ and $DR = 0.5$), generations 15 and 18 (Fig 4), there are two stagnation points: one on the left wall and one on the upper wall (Fig. 5). Conversely, in case 4 ($AR = 0.5$ and $DR = 0.5$), generations 15 (Figs 4), there is only one saddle point near a wall; the left wall (Fig. 5). A saddle point is unnecessary on the top wall in this case because the two smaller closed streamlines are themselves encircled by a larger closed streamline. Nonetheless, there is a second stagnation point in the flow of case 4. This stagnation point is located in the centre of the cavity where the two smaller recirculation regions meet. A similar stagnation point also occurs in the corresponding rigid-wall model. It is noted that the saddle points near the walls are exceedingly close to the wall surface. Specifically, in generation 15 of cases 3 and 4 (Fig. 5) they are typically located at a distance of the order of 0.5% of the alveolar width from the solid surface. Further, cases 1 and 2 also exhibited a single stagnation saddle point very near the left wall in generations with recirculating flow (results not shown), which are similar in location to that shown by Tsuda et al., (1995).

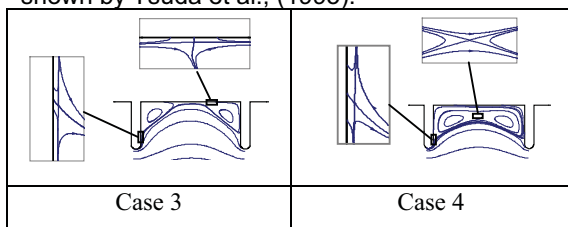


Figure 5. Flow stagnations points in expanding case 3 (left) and case 4 (right) at generation 15 ($AR = 0.5$, $DR = 0.5$). See Table 1 for flow details.

Of the four cases considered, the streamline patterns for case 4 ($AR = 0.5$ and $DR = 0.25$) undergo the most change from entrance region to generation 18 (Fig. 4). Specifically, the encircling streamline seen in the entrance alveolus (Fig 4) disappears at generation 18 (Fig. 4). That is, at generation 18, the streamline pattern of cases 4 is topologically similar to that in case 3 (both have stagnation saddle points near the top and left walls). Conversely, in their entrance alveoli, the flows are plainly dissimilar (case 3 has two near-

wall saddle points and case 4 has one near-wall saddle point and one in the centre of the flow).

As instantaneous streamline patterns do not provide a complete sense of the dynamics of these flows, we also calculated tracks of fluid particle pairs, using a purpose-built tracking program (Henry et al., 2002), in generation 18 of all four geometry cases (Fig. 6). At the beginning of the first breath, each pair of particles was placed just below the proximal septa in a region, found by trial and error, which ensured that both particles remained in the alveolus. The particle pairs were initially separated by a distance equal to 0.2% of the septa width. It was found that the time history of the distance separating the two particles was a function of the case geometry. While the time histories for cases 1 and 2 were quite similar, those for cases 3 and 4 differed from each other and from cases 1 and 2 (Fig. 6).

4. DISCUSSION

We are primarily interested in the dynamics of the flow in alveoli because they can have a profound affect on the transport and deposition of nano-sized particles in the acinus. This is because the diffusivity of such particles is extremely small (typically, four to five orders of magnitude smaller than that of oxygen) and hence they tend to be follow the path taken by the fluid. We note that the flow pattern in the alveoli is of little consequence to gas transport, because, in this case, diffusion transport dominates. This can be shown easily by considering the diffusional length scale $\ell_d \approx \sqrt{Dt}$, which for oxygen is of the order of 7mm (taking $t = T/2 = 2s$), or 70 times the model alveolar width. In contrast, ℓ_d for a 500nm particle is approximately one-tenth the alveolar width.

Radial transport of axial momentum from the duct flow to the alveolar flow is the principle mechanism responsible for the difference between the flow in the alveoli of generation 15 and that of generation 23 (Henry & Tsuda, 2010). For cases where the axial momentum in the duct is high; i.e., in the acinar entrance region, the axial momentum will be converted to angular momentum, by the existence of the distal septum, and rotating flow will occur in the alveoli (Fig 3, gen. 15). Conversely, in areas where the axial momentum in the duct is low; i.e., in the peripheral region, the alveolar flow will be mainly radial (Fig 3, gen. 23). In the expanding models, the radial transport has two components: diffusional and convective. The diffusional transport depends on the kinematic viscosity of air; whereas, the convective component is due to the expanding volume of the alveoli. In the case of the rigid models, the radial transport is purely diffusional.

Henry and Tsuda (2010) showed that radial transport of axial momentum must be dominated by diffusion but this does not hold for the radial transport of nanoparticles. As noted above, the diffusivity of a 500nm particle is five orders of magnitude smaller than the kinematic viscosity of

air. The relative magnitudes of convective and diffusive radial transport of particles can be characterized by a radial Péclet number, $Pe_r = U_r w / D_p$, where D_p is the particle diffusivity. In the case of a 500nm particle, Pe_r ranges from 14 for case 4 to 45 for case 1. Hence, nanoparticles will be largely convected into the alveoli by the expansion of the alveolar cavity.

As submicron particles have negligible inertia, are too small to be significantly affected by gravity and, as shown above, are little affected by diffusion they will tend to follow the same path as the fluid particles. Hence, the fluid particle tracks given in Fig. 6 also give a reasonable estimate of the paths taken by nanoparticles, at least those at the larger end of the scale. We see that, in all cases considered, the particles that enter the alveoli do so over a small area situated very close to the septum tip (Fig. 6). That is, at each generation, a thin annulus of particles is skimmed off from the main duct flow. The thickness of the annulus relative to the duct radius is directly related to QA/QD. Hence, as the acinar periphery is approached the percentage of flow/particles entering the alveoli grows.

The differences in flow structure between the fully developed alveoli (cases 1 and 2) and the less developed ones (cases 3 and 4) produce marked differences in particle path patterns (Fig 6). Nonetheless, in all cases, the particles tend to travel around the flow recirculation regions. Therefore, the particles spend a large part of each breathing cycle reasonably close to the alveolar surfaces. We note that, in general, the particle paths are closer to the alveolar surface opposite the alveolar opening in cases with relatively large values of DR (cases 1 and 3, Fig. 6) than in the cases with smaller DR (cases 2 and 4, Fig. 6). While diffusive transport is small, it can be shown that over a 2s inhalation, the diffusional lengths scale $\approx \sqrt{D_p t}$ of a 500nm particle is equal to roughly one tenth of the alveolar width. Hence, such particles traveling along paths shown in Fig. 6 could migrate to the alveolar surface.

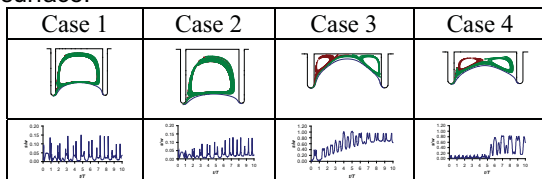


Figure 6. Upper: Tracks of particle pairs over ten breathing cycles. Lower: Time histories of the distance between particle pairs, s , normalized by the alveolar width, w . All at generation 18. Particles initially separated radially, by a distance equal to 0.2% of the septum width, just below the proximal septum. Included is the track of the particle that just grazes the distal septum (blue line).

The main duct flow (i.e., that part of the duct flow that enters the alveoli but is above the path line shown in blue in Fig. 6) of the cases with

aspect ratios of 0.5 (cases 3 and 4) enters deep into the alveoli. Thus the alveolar surfaces of these cases are more exposed to the possibility of deposition of particles from the main flow than are the alveolar surfaces of the fully developed cases (cases 1 and 2). Hence, it could be concluded that the rate of deposition of nanoparticles is higher in the developing lung than in the adult case, at least for the region of the acinus in which recirculating flow occurs in the alveoli; that is, the proximal region.

5. CONCLUSION

We have examined the influence of various features of acinar geometry on the structure of the flow in a typical alveolus in selected generations of a typical human acinus. We have confirmed that acinar flow is quasi steady and that the character of the flow in an alveolus is affected by the ratio of the flow entering the alveolus to that passing by in the duct, the alveolus aspect ratio and the alveolar depth to duct diameter ratio. Using the predicted flow fields, we tracked fluid particle paths over multiple breathing cycles to reveal marked differences between particle paths in fully developed alveoli and those in developing alveoli. Using the particle tracks and order-of-magnitude arguments for the relative strengths of convective and diffusive transport, we suggest that the proximal region of the developing lung could be more susceptible to high rates of nanoparticle deposition compared to the adult counterpart.

ACKNOWLEDGMENT

This study was supported by NIH Grants HL054885, HL070542 and HL074022.

REFERENCES

- [1] Henry, F.S., Tsuda, A., "Radial transport along the human acinar tree," *J Biomech Eng.* 2010, 132(10):101001.
- [2] Tsuda, A., Henry, F.S., Butler, J.P., "Chaotic Mixing of Alveolated Duct Flow in Rhythmically Expanding Pulmonary Acinus," *J. Appl. Physiol.*, 1995, 79(3), pp. 1055–1063.
- [3] Henry, F.S., Butler, J., Tsuda, A., "Kinematically Irreversible Flow and Aerosol Transport in the Pulmonary Acinus: a Departure from Classical Dispersion Transport," *J. Appl. Physiol.*, 2002, 92, pp. 835–845.
- [4] Karl A., Henry F.S., Tsuda, A., "Low Reynolds Number Viscous Flow in an Alveolated Duct," *J. Biomech. Eng.*, 2004, 126, pp. 420-429.
- [5] Weibel, E.R., "The Pathway for Oxygen- Structure and Function in the Mammalian Respiratory System," Harvard University Press, Cambridge, MA. 1984.

Mining Data from Hemodynamic Simulations for Human Aorta

Tošović, Milena; Radović, Miloš; Petrović, Dejan; Milašinović, Danko; Devedžić, Goran; Ranković, Vesna; and Filipović, Nenad

Abstract— To analyze the influence of geometric parameters and flow on maximal wall shear stress (MWSS), maximum pressure and total force in the human aorta, the computer simulations were run to generate the data pertaining to this phenomenon. These data were used for training and testing two data mining models: multilayer perceptron neural network trained with backpropagation algorithm and k-nearest neighbor algorithm. The results showed that both models have strong ability in predicting target variables.

Index Terms — k-nearest neighbor (k-NN), multilayer perceptron neural network (MLPNN), backpropagation algorithm, CFD simulation.

1. INTRODUCTION

ABDOMINAL aortic aneurysm is the most common form of the aortic aneurysm. An aneurysm is the abnormal widening of aorta with increasing more than 50% of the normal diameter. Over time due to blood flow, aortic wall becomes weaker and more stretched, thinner and thicker in the form of balloon.

Patient specific modelling of the blood flow through the human aorta performed using computational fluid dynamics (CFD) and magnetic resonance imaging (MRI) is shown in [1,2].

In order to assess an individual's stroke risk, three-dimensional numerical simulation of blood flow in the aortic arch during cardiopulmonary bypass has been done [3].

The relationship between flow and geometric parameters was observed in the earlier simulated blood flow [4]. Alterations in arterial geometry affect blood flow, shear stress and pressure. Similarly encouraging results are

obtained for the comparison of simulated and measured flow structure [5].

This paper describes how we can predict and analyze state of aorta by using data mining. Many parameters such as pressure, shear stress and force, have an impact on the burden of the aorta.

Our study consisted of several parts. At one side we have trained and tested two different models: neural network trained with backpropagation algorithm and nearest neighbor model. Both methods gave good results with minimal errors. Second part of our research included real patient data. We generated 3D model of aorta for an individual patient, which is then discretized with a set of elements of the same type to perform calculation providing details for conclusion about the process. The best results for fluid gave elements with eight nodes. The results showed that data mining can be used on a real model.

2. METHODS

Our investigation showed that nearest neighbor method and multilayer perceptron neural network can model relationships between geometry parameters and flow data on one side and intensity of the total force, the maximum wall shear stress and the maximum blood pressure on the other side. Set of candidate geometries with different flow values were randomly created for steady state. By running computer simulations total force, MWSS and maximum pressure were calculated. Nearest neighbor method and multilayer perceptron neural network have been created with randomly generated data which approximated total force, MWSS and maximum pressure as a function of geometry and flow.

2.1 Finite Element Model of the Aorta

Figure 1 shows a simplified geometry of the aorta. This geometry was used to generate the blood vessel internal surfaces. For the certain values of input data: geometry and flow, the specific outputs data are calculated: the total force, the maximum wall shear stress and the maximum pressure.

Manuscript received April 5, 2011. The part of this research is supported by Ministry of Science in Serbia, Grant ON174028.

M. Tošović, is with ComTrade ITSS, Kragujevac, Serbia and Faculty of Mechanical Engineering, Kragujevac, Serbia (e-mail: milenakg05@live.com).

N. D. Filipović, is with the Faculty of Mechanical Engineering, Kragujevac, Serbia and Research and Development Center for Bioengineering "BioIRC", Kragujevac, Serbia (e-mail: fica@kg.ac.rs).

G. Devedžić and V. Ranković, are with the Faculty of Mechanical Engineering, Kragujevac, Serbia (e-mail: devedzic@kg.ac.rs, vesnar@kg.ac.rs).

M. Radović, D. Milašinović and D. Petrović are with the Research and Development Center for Bioengineering "BioIRC", Kragujevac, Serbia (phone: 381-34-301920; fax: 381-34-500089; e-mail: mradovic@kg.ac.rs, dmilashinovic@kg.ac.rs and racanac@kg.ac.rs).

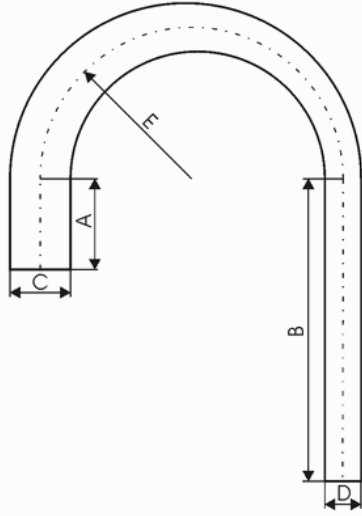


Figure 1: Geometric data for the model of the aorta: A - small height, B - large height, C - large diameter, D - small diameter, E - radius

Using these geometric parameters, flow for blood domain is generated by the finite element model. Simulations in steady state were done for 2000 geometries with different flow values. The total force, the maximum shear stress and the maximum pressure were extracted in order to construct multilayer perceptron neural network and nearest neighbor model.

2.2 Data Set for Modeling MWSS, Total Force, and Maximum Pressure

To demonstrate applicability of data mining techniques for assessing relationships between geometric parameters and flow on the one hand and MWSS, total force and pressure on the other, data set containing 2000 different examples is created. Table 1. shows mean values of six input variables. The perturbation of each parameter was taken as 30% of the corresponding mean value.

TABLE 1: THE AVERAGE VALUES OF INPUT PARAMETERS, GEOMETRIC PARAMETERS ARE EXPRESSED IN METERS, AND FLOW IN m^3/s

| Description | Mean value |
|--------------------|------------|
| Small height (A) | 0.03 |
| Large height (B) | 0.15 |
| Large diameter (C) | 0.023 |
| Small diameter (D) | 0.0185 |
| Radius (E) | 0.05 |
| Flow | 8.333e-005 |

2.3 K-Nearest Neighbor Algorithm

K nearest neighbors algorithm (k-NN) belongs to a class of lazy learning methods. When a new example is presented to a nearest neighbor predictor, a subset of learning examples most similar to the new example is used to make a prediction. This method is described in [6,7].

For regression problems the mean target variable value from the set of nearest neighbors is predicted:

$$c_x = \frac{1}{k} \sum_{i=1}^k c_i \quad (1)$$

where k is the number of nearest learning examples which influence the prediction of k-NN algorithm.

Type of distance measure has big impact on determining which set of learning examples are closest to the new example. In the most cases, Euclidean distance is used:

$$D(t_i, t_j) = \sqrt{\sum_{i=1}^a d(v_{i,l}, v_{i,j})^2} \quad (2)$$

Before calculating Euclidean distance all attributes are scaled to the [0,1] interval. For continuous attributes (which is our case) the distance between two attributes $v_{i,l}$ and $v_{i,j}$ is defined as:

$$d(v_{i,l}, v_{i,j}) = |v_{i,l} - v_{i,j}| \quad (3)$$

2.4 Multilayer perceptron neural network

Multilayer perceptron neural network (MLPNN) is composed of simple elements called *neurons*. The basic structure of the MLPNN, consists of one or more hidden layers and an output layer.

The objective of the training is to find a set of weights and biases that minimize the error between the neural network predictions and the desired outputs. There are different learning algorithms. The back-propagation algorithm [8] has been the most commonly used training algorithm. The basic algorithm is a gradient descent method in which the network weights and biases are moved along the negative performance function. One iteration of this algorithm can be written as:

$$\Delta X = lr \cdot \frac{dperf}{dX} \quad (1)$$

where X represents weight and bias variables of the network, lr is learning rate and $perf$ is performance function which defines how much real outputs disagree with predicted ones (mean squared error for example).

It has problems with local minima and slow convergence. In the literature, a number of variations of the standard algorithm have been developed [9]. In this study we used backpropagation algorithm with momentum and adaptive learning rate. Each variable is adjusted according to gradient descent with momentum:

$$\Delta X = m_c \cdot \Delta X_{prev} + lr \cdot m_c \cdot \frac{dperf}{dX} \quad (2)$$

where m_c is momentum constant and ΔX_{prev} is the previous change of the weight or bias. For each epoch, if performance decreases toward the goal, then the learning rate is increased by the lr_{inc} factor. If performance increases by more than the max_{inc} factor, the learning rate is adjusted by the factor lr_{dec} and the change that increased the performance is not made. The

values of m_c , lr_{inc} , lr_{dec} and \max_{inc} are given in table 3.

TABLE 3: m_c , lr_{inc} , lr_{dec} AND \max_{inc} VALUES USED FOR MULTILAYER PERCEPTRON TRAINING

| m_c | lr_{inc} | lr_{dec} | \max_{inc} |
|-------|------------|------------|--------------|
| 0.9 | 1.05 | 0.7 | 1.04 |

MLPNN with as few as one single hidden layer is indeed capable of universal approximation in a very precise and satisfactory sense [10].

There are several different criteria for learning stop (maximum number of epochs, maximum amount of time, performance goal, etc.). In this study we used maximum number of learning epochs (1000).

2.5 3D Reconstruction

Our study also included creating 3D model of aorta based on scanned images for one patient. For this purpose Mimics and Geomagic software were used. This model presented network of equilateral triangles. The model is discretized with array of elements of same type, array of tetrahedrons. Fluid domain was meshed via meshing software FEMAP. From triangles we got tetrahedrons which are 3D objects that perfectly lie on each other (shown in Figure 2).

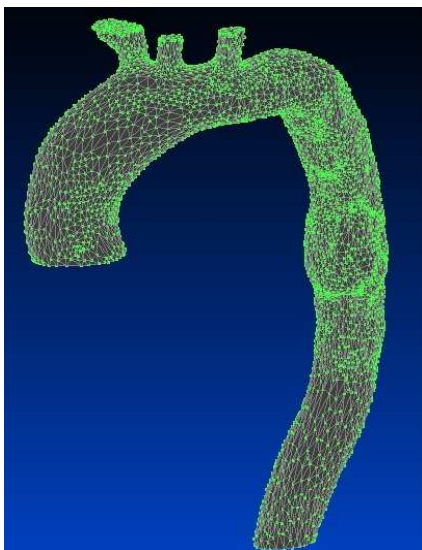


Figure 2: Model of the aorta filled with tetrahedrons

These tetrahedrons fill volume of aorta. By division of one tetrahedron on four parts we got elements with eight nodes, bricks. The reason for new division is that elements with eight nodes give the best results for fluid, in our case for blood. These elements will be inputs for solver, program which calculate parallel algorithm on parallel computers. Results are the vectors point domain. From these results we can conclude about behavior of the aorta.

3. RESULTS

In our example we used K-nearest neighbor algorithm and multilayer perceptron neural network trained with backpropagation algorithm.

For testing leave-one-out cross validation is used where in each iteration one of 2000 examples acts as a test example on the model which is built on the remaining 1999 examples.

We evaluated the performance of the models by computing their relative mean squared error (RMSE) and relative absolute error (RAE). RMSE is computed as a mean squared difference between the true and the predicted values of the outputs for each of 2000 examples in the data set and is afterwards normalized with the mean squared error of the default predictor (i.e. a model which always predicts an average value of the output).

$$RMSE = \frac{\sum_{i=1}^n (f_i - \hat{f}_i)^2}{\sum_{i=1}^n (f_i - \bar{f})^2} \quad (6)$$

where \bar{f} is an average output value.

Similar, RAE is computed as a mean absolute difference between the true and the predicted values of the outputs for each of 2000 examples in the data set and is afterwards normalized with the mean absolute error of the default predictor.

$$RAE = \frac{\sum_{i=1}^n |f_i - \hat{f}_i|}{\sum_{i=1}^n |f_i - \bar{f}|} \quad (7)$$

The values of RMSE and RAE smaller than 1.0 indicate that the model is useful. The lower RMSE and RAE are, the more accurate the model is. The RMSE and RAE values for the multilayer perceptron and k-NN algorithm are shown in tables 3 and 4 respectively. From these tables we can see that both, MLPNN and k-NN models, showed high potential in this prediction task. Also, we can see that neural network model showed higher precision in this precision task than k-NN model.

Multilayer perceptron with 5 neurons in hidden layer, sigmoid activation functions in hidden neurons and linear activation function in the output neuron is used (Figure 3). The stopping criterion was defined as the maximum number of learning epochs (1000). The number of neurons in the input and output layer is determined by the problem we are solving. In our case we have six input neurons corresponding to six input parameters (see table 1) and three output neurons corresponding to total force, MWSS and max pressure. Preprocessing of data has been performed where inputs and outputs are scaled to the interval [-1,1].

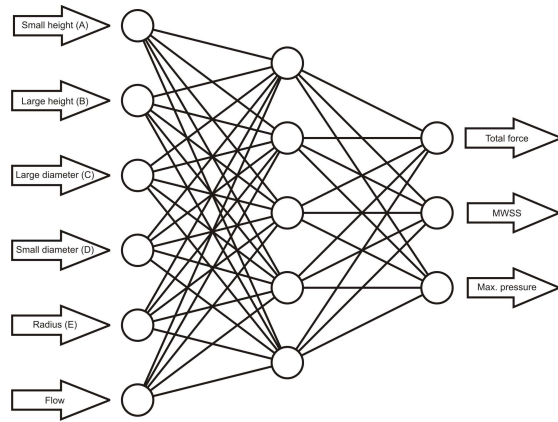


Figure 3: Structure of MLPNN

K-nearest neighbors algorithm predicts the target value that is averaged from the 5 most similar learning examples (nearest neighbors) in the problem space ($k=5$).

TABLE 3: RESULTS OF PREDICTING TOTAL FORCE, MWSS, MAX PRESSURE USING MULTILAYER PERCEPTRON

| ERROR | Total Force intensity | MWSS | Max Pressure |
|-------|-----------------------|--------|--------------|
| RMSE | 0.0266 | 0.0469 | 0.0342 |
| RAE | 0.1464 | 0.1939 | 0.1642 |

TABLE 4: RESULTS OF PREDICTING TOTAL FORCE , MWSS, MAX PRESSURE USING K-NEAREST NEIGHBOR ALGORITHM

| ERROR | Total Force intensity | MWSS | Max Pressure |
|-------|-----------------------|--------|--------------|
| RMSE | 0.0551 | 0.0875 | 0.0834 |
| RAE | 0.2063 | 0.2549 | 0.2316 |

By using computer simulation we have calculated the total force, MWSS and maximum pressure for real example. Then, we tried to predict these values by using multilayer perceptron and nearest neighbor method. These results are compared in table 6. The geometric parameters for real example are measured (Figure 4) and values are presented in table 5.

TABLE 5: INPUTS FOR REAL EXAMPLE, GEOMETRIC PARAMETERS ARE EXPRESSED IN METERS, AND FLOW IN m^3/s

| Description | Value |
|--------------------|------------|
| Small height (A) | 0.038 |
| Large height (B) | 0.174 |
| Large diameter (C) | 0.029 |
| Small diameter (D) | 0.021 |
| Radius (E) | 0.0488 |
| Flow | 8.333e-005 |

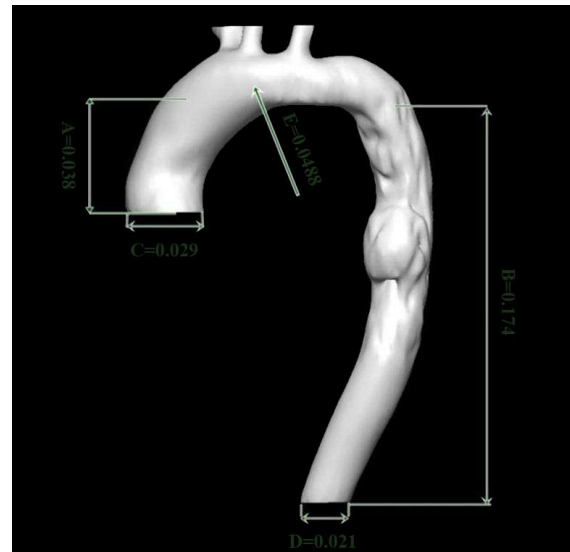


Figure 4: Real example geometry

Figures 5 and 6 show wall shear stress and pressure distribution respectively. These results are obtained by using solver for 3D reconstruction.

TABLE 6: REAL EXAMPLE RESULTS

| | Total Force intensity | MWSS | Max Pressure |
|------------|-----------------------|-----------|--------------|
| Real value | 2.02e-002 | 4.18e+002 | 2.13e+004 |
| MLPNN | 1.87e-002 | 3.76e+002 | 2.02e+004 |
| K-NN | 2.02e-002 | 4.07e+002 | 2.13e+004 |

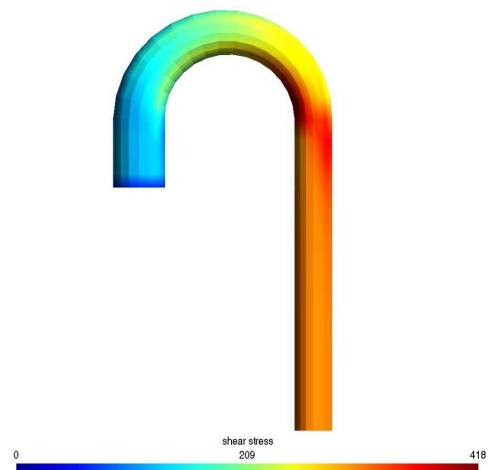


Figure 5: Wall shear distribution for real example

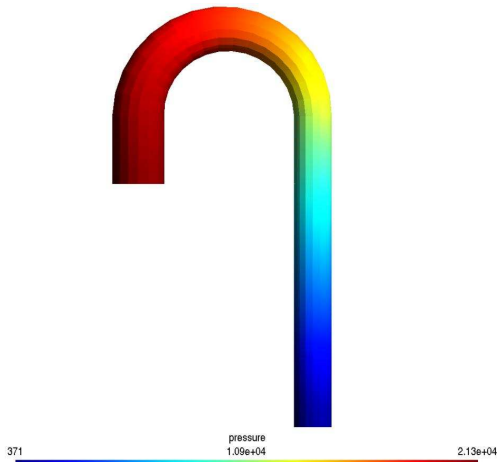


Figure 6: Pressure distribution for real example

4. DISCUSSION AND CONCLUSION

The purpose of this work was to find correlation between geometry and flow data inside aortic blood flow and hemodynamics parameters (total force, MWSS and maximum blood pressure). The applied methodology was data mining approach. In this study we implemented two different data mining algorithms: backpropagation and nearest neighbor algorithm. Both algorithms have shown very good results. If we compare the results from tables 3 and 4, we can conclude that the K-nearest neighbor algorithm gives slightly better results than backpropagation algorithm for the multilayer perceptron. It is also shown that these two models can be applied on real patient model. Further research will include testing other regression algorithms, like linear regression and support vector machine, for this problem. Also, we will compare performance of the used neural network with the performance of three individual networks, each having a single output neuron for different predictive task.

ACKNOWLEDGMENT

This work is part funded by European Commission (Project ARTREAT, ICT 224297).

REFERENCES

- [1] Svensson, J., Gårdhagen, R., Heiberg, E., Ebbers, T., Loyd, D., Länne, T., Karlsson, M., "Feasibility of Patient Specific Aortic Blood Flow CFD Simulation," MEDICAL IMAGE COMPUTING AND COMPUTER-ASSISTED INTERVENTION – MICCAI 2006, Lecture Notes in Computer Science, 2006, 4190/2006, pp. 257-263.
- [2] Keisuke, F., Daisuke, M., Tomoaki, H., Takami, Y., Liu, H., "Modeling and CFD simulation of the human aortic arch based on the MRI image," Nihon Kikai Gakkai Nenji Taikai Koen Ronbunshu, 2000(1), pp. 265-266.
- [3] Tokuda, Y., Song, M.h., Ueda, Y., Usui, A., Akita, T., Yoneyama, S., Maruyama, S., "Three-dimensional numerical simulation of blood flow in the aortic arch during cardiopulmonary bypass," European Journal of Cardio-thoracic Surgery, 33, pp. 164–167, 2008.
- [4] Shahcheraghi N., Dwyer, H.A., Cheer, A.Y., Barakat, A.I., Rutaganira, T., "Unsteady and three-dimensional simulation of blood flow in the human aortic arch," ASME Journal of Biomechanical Engineering 2002.
- [5] Wood, N.B., Weston, S.J., Kilner, P.J., Gosman, A.D., Firmin, D.N., "Combined MR imaging and CFD

- simulation of flow in the human descending aorta," Journal of Magnetic Resonance Imaging, 2001.
- [6] Kononenko, I., Kukar, M., "Machine learning and data mining," Horwood Publishing Chichester, UK, 2007.
- [7] Aha, D., Kibler, D., "Instance-based learning algorithms. Machine Learning," Kluwer Academic Publishers, Boston, 6, pp. 37–66, 1991.
- [8] Rumelhart, D.E., Hinton, G.E., Williams, R. J., "Learning internal representations by error propagation," MIT Press, Cambridge, MA, USA, pp. 318-362, 1986.
- [9] Haykin, S., "Neural Networks: A Comprehensive Foundation," Prentice Hall, New Jersey, USA, 1999.
- [10] Hornik, K., "Approximation capabilities of multilayer feedforward networks," *Neural network*, 1991, 4(2), 251–257.

A Back Spine Position Measuring System based on Accelerometer Data

Peulic, Aleksandar; Högl, Hubert; Filipovic, Nenad; and Zoran Ebersold

Abstract—This paper describes a microprocessor system for on board signal acquisition to determine range of motion values of lumbar spine. Wavelet transform was performed for filtering and processing of acquired signals. We present a wearable, unobtrusive system for real-time data monitoring, which consists of off-the-shelf components and sensors. The wavelet transform is showing itself as a useful mathematical tool in the field of signal compression system and there is an increasing need in many data acquisition applications for having a development environment which could be flexible enough for specific measuring systems. An elementary example of a wavelet transform using the matrix algebra approach will be presented. For development we completely use open-source tools, in detail the GNU toolchain for ARM and the OpenOCD debugger. Deformation distribution of the spinal motion segment was determined with finite element analysis. Lateral bending, trunk flexion, extension, pelvic tilts were evaluated in the measurements. The results show the three-dimensional mechanical deformation distribution inside the spinal motion segment during flexion.

Index Terms — Finite element modelling, rehabilitation, sensors designs, wavelet transform.

1. INTRODUCTION

It is essential to know the range of motion (ROM) values for proper rehabilitation procedure after spine part surgery. Also, it is helpful during the rehabilitation treatment to observe the progression of the patients recovery. Various methods and devices are used for motion analysis. Schober technique, radiologic researches, videofluoroscopic analysis, goniometry and inclinometry are the most frequently used [1,2,3]. Nowadays the devices which enable three dimensional motion analysis on the skin have been developed due to technological advance. There are a number of devices such as Moire topography,

pho-togrammetry, video raster stereometry, optoelectronic scanner, ultrasound scanner and cineradiography [4, 5, 6]. Following standard lumbar discectomy, the residual complaints persist to some degree in 28 % to 74.6% of patients and they are common diagnostic and therapeutic problems. Studies have focused on the radiological identification of possible pain-inducing structures in failed back surgery patients. However, recurrent pain following lumbar surgery is clinically often non-specific, and imaging techniques frequently fail to demonstrate a structural reason for the pain. As a consequence, no consensus exists on the management of such residual pain, especially if technical investigations are negative. Exercise therapy following surgery has been shown to have a beneficial effect [7-9], but how rehabilitation programs should be composed remains a controversial issue [8]. Following back surgery, surgical recovery has to be facilitated. During the inflammation phase, the focus in rehabilitation is on the wound healing and on the pain control. The duration of this phase is depending on the surgery performed: the more invasive the surgery, the longer the inflammation phase. Adequate pain relief, with pain killers on schedule, inhibiting break through pain, is essential. Although a lot of surgeons brace their patients postoperatively, there is an obvious lack of consensus regarding indications for immobilization, the most appropriate type of brace and the duration of bracing. In our opinion, the duration of bracing should be kept as short as possible, since it has been shown that lumbosacral orthoses reduce muscle activities in the thoracic and lumbar erector spinae muscles [10].

Wavelet technology encompasses the idea of taking large amounts of data at one end of a process, and being able to store that massive amount of information in a much smaller, more space efficient form at the other end, while at the same time retaining what is necessary to keep the transformed data accurate. The wavelet transformation is a alternative tool to traditional time-frequency representation technique such as the discrete Fourier transform. It is an efficient signal processing technique that can be used to represent real-life non stationary signals. Wavelet transform has been used in many applications such

A. Peulic is with the Department of Electrical Engineering, University of Kragujevac, Serbia, e-mail: apeulic@tfc.kg.ac.rs

Hubert Högl is with the Faculty for informatics, University of Applied Science, Augsburg, Germany, e-mail: Hubert.Hoegl@hs-augsburg.de

Nenad Filipovic is with the Faculty of Mechanical Engineering, University of Kragujevac, Serbia, e-mail: fica@kg.ac.rs

Zoran Ebersold is with the Fujicu Augsburg, PhD student of University of Kragujevac, Serbia, e-mail: ebersold@gmx.net

as image processing and compression, transient signal analysis, numerical analysis, seismic geology, quantum physics and among many other applications. The Discrete Wavelet Transform (DWT) is a useful tool for signal and image processing applications adopted in many emerging standards [11]. Wavelets, as their name implies, are little waves. More specifically, they are oscillatory functions that increase and decrease. Linear algebra approach implemented in our system provides a tool for illuminating some wavelet algorithms and for developing wavelet and scaling function coefficients for the edges of a finite signal.

2. OVERVIEW OF DWT AND COMPUTATIONAL METHODS

Wavelets are function basis sets that can be localized in both real and in Fourier space. The basis is constructed from dilations and translations of the original wavelet function. There are many possible choices for the wavelet function; commonly known wavelets are the Haar and Daubechies-4 wavelets. The wavelet transform expands an signal in terms of the wavelet basis functions. There exists a class of orthogonal wavelet transforms, analogous to Fourier transforms. The wavelet transform (WT) is a decomposition of the signal as a combination of a set of basis functions, obtained by means of dilation a and translation b of a single prototype wavelet $\psi(t)$ where the WT of a signal $x(t)$ is defined as 1:

$$W_a x(b) = \frac{1}{\sqrt{a}} \int_{-\infty}^{\infty} x(t) \psi\left(\frac{t-b}{a}\right) dt$$

The greater the scale factor is, the wider is the basis function and consequently, the corresponding coefficient gives information about lower frequency components of the signal, and vice versa. In this way, the temporal resolution is higher at high frequencies than at low frequencies, achieving the property that the analysis window comprises the same number of periods for any central frequency. If the prototype wavelet $\psi(t)$ is the derivative of a smoothing function $\theta(t)$, it can be shown [12], [13] that the wavelet transform of a signal $x(t)$ at scale a is 2:

$$W_a x(b) = -a \left(\frac{d}{db}\right) \int_{-\infty}^{\infty} x(t) \theta\left(\frac{t-b}{a}\right) dt$$

Where

$$\theta_a(t) = \left(\frac{1}{\sqrt{a}}\right) \theta\left(\frac{t}{a}\right)$$

is the scaled version of the smoothing function. The wavelet transform at scale a is proportional to the derivative of the filtered version of the signal with a smoothing impulse response at scale a . Therefore, the zero-crossings of the WT correspond to the local maxima or minima of the smoothed signal at different scales, and the maximum absolute values of the wavelet transform are associated with maximum slopes in the filtered signal. The scale factor a and/or the translation parameter b can be discrete. The usual choice is to follow a dyadic grid on the time-scale plane:

$$a = 2^k; b = 2^k l$$

The transform is then called dyadic wavelet transform, with basis functions 5:

$$W_{k,l}(b) = 2^{-\frac{k}{2}} \psi(2^{-k} t - l); k, l \in Z^+$$

For discrete-time signals processing, the dyadic discrete wavelet transform DWT is equivalent, according to Mallats algorithm, to an octave filter bank [14], and can be implemented as a cascade of identical cells [low-pass and high-pass finite impulse response FIR filters], as illustrated in 1.

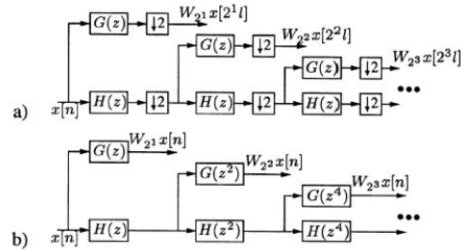


Figure 1: Two filter-bank implementations of DWT (a) Mallats algorithm. (b) Implementation without decimation

From the transformed coefficients

$$W_{2^k} x(2^k l)$$

and the low-pass residual, the original signal can be rebuilt using a reconstruction filter bank. The downsamplers after each filter in 1(a) remove the redundancy of the signal representation. As side effects, they make the signal representation time-variant, and reduce the temporal resolution of the wavelet coefficients for increasing scales. To keep the time invariance and the temporal resolution at different scales, we use the same sampling rate in all scales, what is achieved by removing the decimation stages and interpolating the filter impulse re-sponses of the previous scale. This algorithm, called algorithm trous [15], is shown in fig. 1(b). Using this algorithm, the equivalent frequency response for the k -th scale is 7:

$$Q_k(e^{j\omega}) = \begin{cases} G(e^{j\omega}), & k = 1 \\ G(e^{j2^{k-1}\omega}), \prod_{l=0}^{k-2} H(e^{j2^l\omega}), & k \geq 2 \end{cases}$$

Linear algebra Haar approach: Linear algebra provides a tool for illuminating some wavelet algorithms and for developing wavelet and scaling function coefficients for the edges of a finite signal. In practice matrices are not used to calculate the wavelet transform. Each step in the forward Haar transform calculates a set of wavelet coefficients and a set of averages. If a data set x_0, x_1, \dots, x_{N-1} contains N elements, there will be N/2 averages and N/2 coefficient values. The averages are stored in the lower half of the N element array and the coefficients are stored in the upper half. The averages become the input for the next step in the wavelet calculation. The recursive iterations continue until a single average and a single coefficient are calculated. This replaces the original data set of N elements with an average, followed by a set of coefficients whose size is an increasing power of two. The Haar equations to calculate an average a_i and a wavelet coefficient c_i from an odd and even element in the data set are shown 8:

$$a_i = \frac{x_1 + x_{i+1}}{2}, d_i = \frac{x_1 - x_{i+1}}{2}$$

In wavelet terminology the Haar average is calculated by the scaling function. The coefficient is calculated by the wavelet function. Five level Haar transform for 64 sample width of window is realized by:

```
//
*****
int X_ul[] = acquire_signal[] ;
int buf_a[64]; int buf_d[64];

int Nb_sample=64;

int haar_wav_5(int x, int buf_ul[]);
// main function void main(void)
{
while(1)
{
haar_wav_5(Nb_sample, X_ul); //first step
haar_wav_5(Nb_sample/2, buf_a); //second step
haar_wav_5(Nb_sample/4, buf_a); //third step
haar_wav_5(Nb_sample/8, buf_a); //fourth step
haar_wav_5(Nb_sample/16, buf_a); //fifth step
}
} //end_main
int haar_wav_5(int x, int buf_ul[]){
int i; int j=0;
```

```
for (i=0;i<x; i=i+2){
buf_a[j]=(buf_ul[i]>>1)+(buf_ul[i+1]>>1);
buf_d[j]=(buf_ul[i]>>1)-(buf_ul[i+1]>>1); j=j+1;
} //end for
return buf_a[j],buf_d[j];
}
```

We implemented Finite Element (FE) formulation where the nodal variables are:

- Displacements of solid U,
- fluid pressure P,
- Darcys velocity Q,
- electrical potential .

A standard procedure of integration over the element volume is performed and the Gauss theorem is employed. An implicit time integration scheme is implemented, hence the condition that the balance equations are satisfied at the end of each time step is imposed. The matrices and vectors are 9,10,11,12,13:

$$K_{q\phi} = -k_{11}^{-1}k_{12} \int_V N_q^T N_{\phi,x} dV$$

$$K_{\phi q} = k_{21} \int_V N_{\phi,x}^T N_{q,x} dV$$

$$K_{\phi\phi} = -k_{22} \int_V N_{\phi,x}^T N_{\phi,x} dV$$

$${}^{n+1}F_q = \int_V N_q^T \rho_f^{n+1} b dV - K_{qp}^n P - K_{qq}^n Q - K_{q\phi}^n \phi$$

$${}^{n+1}F_\phi = \int_A N_\phi^T n^T j dA - K_{\phi p}^n P - K_{\phi q}^n Q - K_{\phi\phi}^n \phi$$

Details about all variables in equations are given in [7].

3. ARCHITECTURE AND IMPLEMENTATION

The proposed experimental system integrates wired 3D accelerometer sensors to achieve accelerations three axis data. The system features an ARM 7 processor Atmel AT91SAM7s256 with 256 Kbytes internal high-speed Flash and 64 Kbytes internal high-speed SRAM. The processor runs at 18.432 MHz that allows execution of data acquisition algorithms in real-time, while power efficient modes extend battery life. The system is designed as intelligent 3 degree of freedom sensors and contains a 3D accelerometer ADXL330, fig. 2. The ADXL330 is a small, thin, low power, complete 3-axis accelerometer with signal

conditioned voltage outputs, all on a single monolithic IC. The product measures acceleration with a minimum full-scale range of 3g. It can measure the static acceleration of gravity in tilt-sensing applications, as well as dynamic acceleration resulting from motion, shock, or vibration.

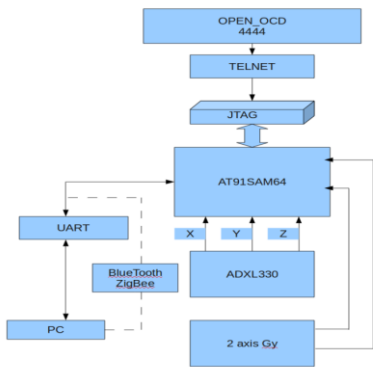


Figure 2: Block diagram of the experimental system

The ARM processor controls sensors and communicates with the capture device, in our case it is a standard PC. Noisy signal fig.3 represents the X axis from the accelerometer components, where Y axis is acceleration in g and X axis number of samples. Direct angle estimate requires inverse tan-tangent function that amplifies noise from accelerometer signals. Simple Haar transform level 1 fig.4 and level 3 fig.5 of the accelerometer signal improves the estimate and de-noises the signal.

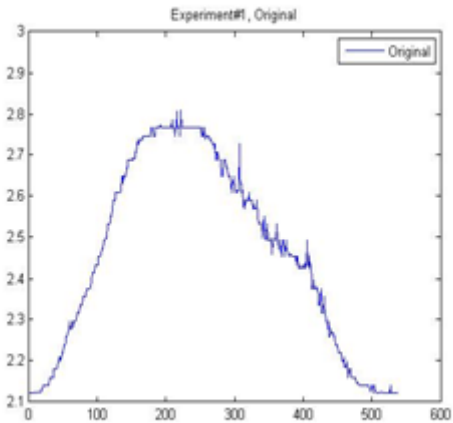


Figure 3: Raw x axis signal in g per samples before wavelet filtering

All signals are sampled at 100 Hz. Output is generated every 10 ms for raw signals, estimated positions for X, Y and Z signals are represented in figure 6. The ARM board is controlled with the OpenOCD debugger as shown in figure 7.

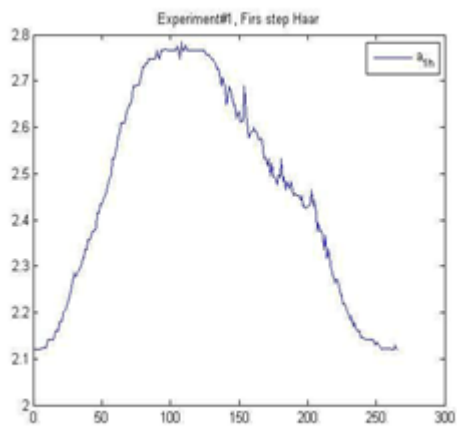


Figure 4: Performed first Haar level, x acceleration axis in g per samples

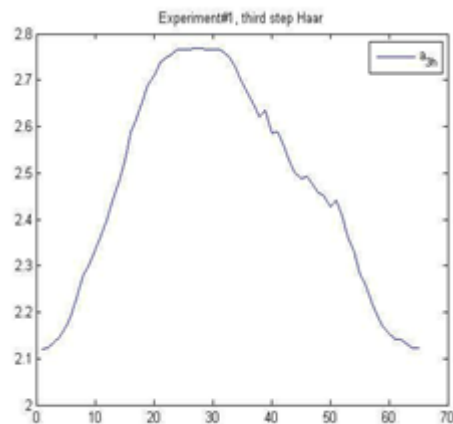


Figure 5: Performed third Haar level, x acceleration axis in g per samples

Calibration of sensors became necessary as we discovered that each inertial sensors axis had different offset and sensitivity. Calibration of the acceleration sensor was done by rotating it to obtain each axis maximum and minimum values for +1g and -1g. Special attention was needed to keep this device in the same plane of rotation.

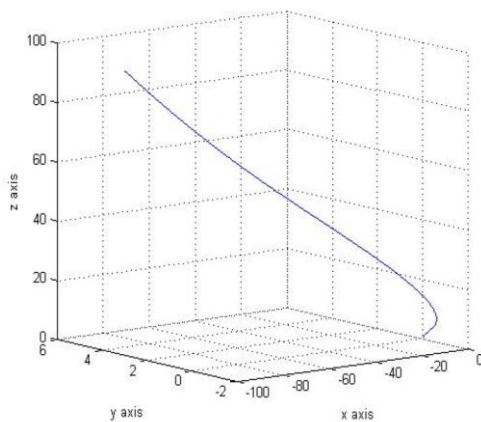


Figure 6: Wearable sensor position in 3D during trunk flexion in [mm]

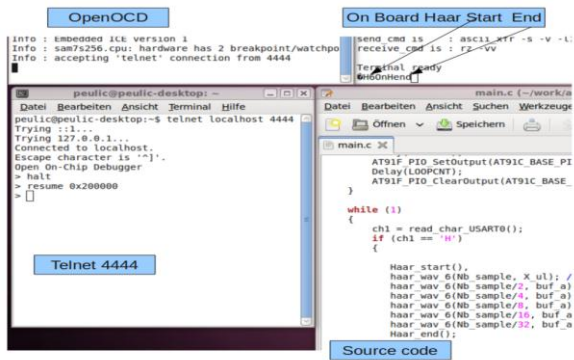


Figure 7: Terminal windows, OpenOCD, telnet, picocom and code

Using these experimental results and values of total angle in flexion and extension we calculated movement of the spine part as it is described. Figure 8 presents SMS computer model before, and Figure 9 SMS deformation distribution after trunk flexion.

Due to free and open-source software it has never been easier to get high-quality cross development software for a broad range of microcontrollers. This application field is mainly dominated by the GNU Compiler Collection GCC, consisting of a C/C++ compiler, assembler, linker and util-ities. Considering especially the ARM architecture, a well-established "arm-gcc" port is available. When it comes to debugging the situation gets worse. The difficulties start when programs shall run on the target processor under control of GDB when restricting oneself to only free software. Many modern controllers like those from ARM have "Embedded

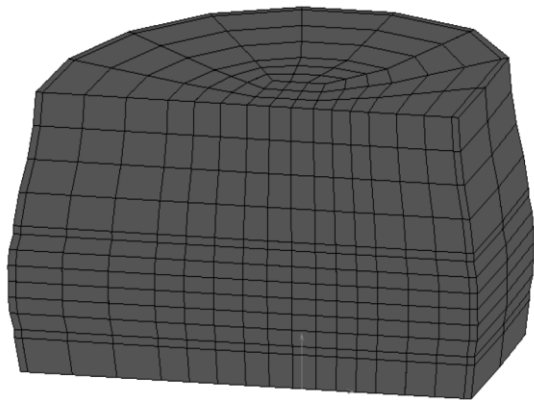


Figure 8: Spinal Motion Segment Computer FE Model before trunk flexion

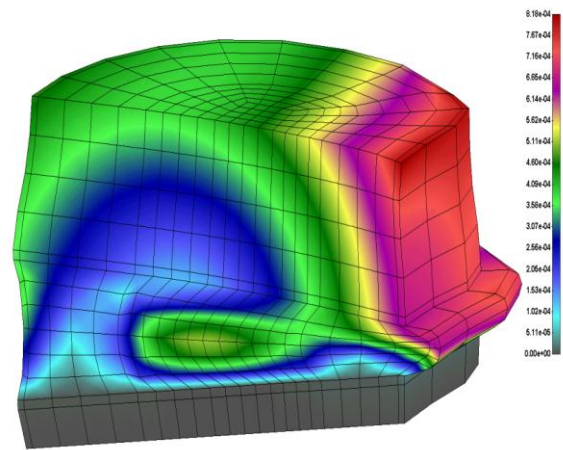


Figure 9: Computer FE Model Deformation distribution of SMS after trunk flexion

ICE" (EICE) facilities on chip to get full control within a debugger over the target program. The EICE is driven by a "JTAG" port, which is a four-wire synchronous serial port accessible at some package pins. The JTAG port is often called "TAP" (Test Access Port). There is GDB, the GNU Debugger. For most architectures GDB comes with a simulator, so that simulating programs written with GCC is in general not a problem. In contrast to the target hardware a plain GDB has no concepts of EICE, JTAG and similar details at the hardware level. GDB's concept of debugging is expressed in a Remote Serial Protocol (RSP) which is a simple ASCII high-level protocol to control the debug process. For example for a memory modify operation GDB will emit the string M4015cc,2:c320#6d (address 0x4015cc, size 2 bytes, data 0xc320; the value 6d after # is a checksum). The RSP specification is contained in the GDB documentation. The necessary piece of software between tool-chain and target is in principle a protocol converter from RSP to JTAG bitstream commands (fig.10).

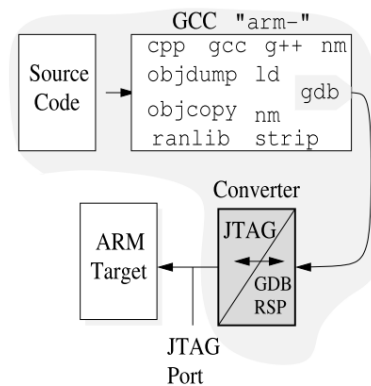


Figure 10: The GNU Toolchain, enhanced with the GPL'ed OpenOCD converter between GDB/RSP and JTAG bitstream commands. Everything on the gray background runs on the development (host) computer

Linux, MacOS/X, Windows

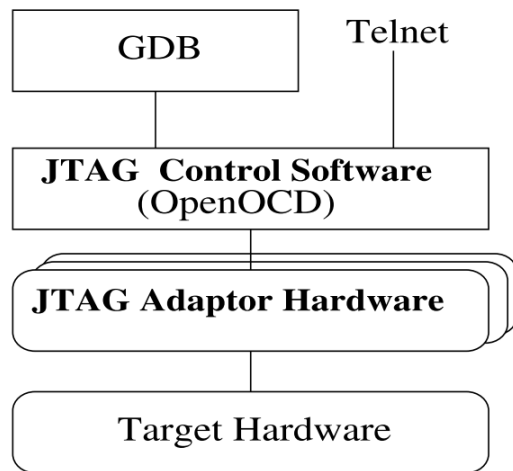


Figure 11: More detailed interfaces when debugging with GDB and OpenOCD

In more detail, debugging target code in GDB via JTAG consists of the interfaces shown in fig. 11. OpenOCD opens two network connections for GDB/RSP and Telnet. The debugger and the OpenOCD server can thus be run on different machines. New JTAG adaptors can be easily added to OpenOCD.

4. CONCLUSION

We presented an approach for a real-time acquisition system based on wavelet transform processing. In addition we proposed an approach to position monitoring. The Daubechies wavelet transforms are defined in the same way as the Haar wavelet transform by computing the running averages and differences via scalar products with scaling signals and wavelets. The only difference between them consists in how these scaling signals and wavelets are defined and we plan to implement the Daubechies wavelet transforms in our system. The proposed system is very convenient for medical applications, unobtrusive, real-time monitoring, computer assisted physical rehabilitation, such as post-surgery and stroke rehabilitation, real time walking monitoring, freezing gate monitoring in Parkinson's disease and in industrial applications such as robotic and mechatronics systems. We plan to expand our system to full on-board processing and support simultaneous monitoring of multiple objects. Medical doctors involved in treatments could share experience and knowledge. Future work will include clinical experiments on the larger set of patients at Clinic Centre as well as more complex FE model with more coupled SMS. Also the larger number of patients will provide ability to more effectively analyse. We plan to experiment with different sensors, custom sensors and radio modules. Also we plan on board analysis and data processing using a different microcontrollers core.

ACKNOWLEDGMENT

This research was supported by Ministry of Science of Serbia TR12007, and OI144028 and DAAD Germany research grant.

REFERENCES

- [1] Mellin, G. and Kiiski, R. and Weckstrom, A., , Effects of subject position on measurements of flexion, extension and lateral flexion of the spine, Spine, 1991.
- [2] Pearcy, M. and Portek, I. and Shepherd, J., , The effect of low-back pain on lumbar spinal movements measured by threedimensional X-ray analysis, Spine, 1985.
- [3] Wong, KW. and Luk, KD. and Leong, JC. and Wong, SF., , Assessing lumbar sagittal motion using videography in an in vivo pilot study, Int J Ind Ergon, 2007.
- [4] Filiz, M. and Cakmak, A. and Ozcan, E., , The effectiveness of exercise programmes after lumbar disc surgery: a randomized controlled study, Clinical Rehabilitation, 2005.
- [5] Yilmaz, F. and Yilmaz, A. and Merdol, F. and Parlar, D. and Sahin, F. and Kuran, B., , Efficacy of dynamic lumbar stabilization exercise in lumbar microdiscectomy, Journal of Rehabilitation Medicine, 2003.
- [6] Cholewicki, J. and Reeves, NP. and Everding, VQ. and Morrisette, J., , Lumbosacral orthoses reduce trunk muscle activity in a postural control task, Biomechanics, 2007.
- [7] Kojic, M. and Filipovic, N. and Stojanovic, B. and Kojic, N., , Computer modeling in bioengineering, Theoretical background, examples and software, John Wiley and Sons, 2008.
- [8] Ostelo, RW. and deVet, HCW. and Waddell, G. and Kerckhoffs, MR. and Leffers, P. and van Tulder, MW., , Rehabilitation after lumbar disc surgery (Cochrane Review). In: The Cochrane Library, John Wiley and Sons, 2004.
- [9] Frank, E.H. and Grodzinsky, A., , Cartilage electromechanics-II. A continuum model of cartilage electrokinetics and correlation with experiments, Journal of Biomechanics, 1987.
- [10] Plagenhoef, S., , Computer programs for obtaining kinetic data on human movement, Journal of Biomechanics, 1978.
- [11] Werner Bani, "Wavelets – Eine Einfuhrung" fur Ingenieure, Munchen, Wien, ISBN 3-486-25427-8, 2002.
- [12] S. Mallat and S. Zhong, Characterization of signals from multiscale edge, IEEE Trans. Pattern Anal. Machine Intell., 1992.
- [13] J. S. Sahambi, S. Tandon, and R. K. P. Bhatt, Wavelet based ST-segment analysis, Comput, 1998.
- [14] S. Mallat, Multifrequency channel decompositions of images and wavelet models, IEEE Trans. Acoust. Signal Processing, 1989.
- [15] S. Mallat, A. Cohen and J. Kovacevic, Proc. IEEE, 1996.

The Investigation of Flow – Structural Interaction in an Arterial Branching by Numerical Simulation

Alin A. Dobre, *Student Member, IEEE*; Alexandru M. Morega, *Senior Member, IEEE*; and Mihaela Morega, *Member, IEEE*

Abstract—*There is an outstanding growing interest in developing numerical methods and tools to investigate the hemodynamic of the arterial flow, and to understand its interaction with the anatomic structural system. As arteries morphology is complex and patient-related, medical data based reconstruction of the geometry may be utilized to generate realistic computational domains. Numerical methods and image-based geometry reconstruction have reached the stage where they may be utilized to investigate and predict the hemodynamic flows in arteries. In this paper we report numerical simulation results on arterial blood flow – vessel and muscular mass interaction. The flow patterns and the structural displacements thus obtained may be utilized for vascular surgery training, planning and intervention, to investigate atherosclerosis genesis, in drug targeting, etc.*

Index Terms—*Medical image reconstruction, numerical simulation, arterial flow*

1. INTRODUCTION

CARDIOVASCULAR disease has serious health and social consequences for individuals while forcing the health care system to significant financial effort. According to statistical surveys [1] modern civilized populations suffer in an increasing rate, even from early ages, of Coronary Heart and Peripheral Arterial Diseases (CHPAD), associated to and favored by Arteriosclerotic Vascular Disease (ASVD) syndrome, more frequently called *atherosclerosis* [2]. A major

The work was conducted in the Laboratory for Electrical Engineering in Medicine (IEM) – Multiphysics Models, the BIOINGTEH platform, at the University POLITEHNICA of Bucharest. A. M. Morega acknowledges the support offered by the research grant CNCSIS PCCE-55/2008. A. A. Dobre acknowledges the support offered by the POSDRU/88/1.5/S/61178 grant.

A. A. Dobre is a graduate student of the Faculty of Electrical Engineering, University POLITEHNICA of Bucharest, Bucharest, CO 060042, Romania. (e-mail: alin_dobre@yahoo.com).

A. M. Morega is with the Faculty of Electrical Engineering at the University POLITEHNICA of Bucharest, Bucharest, CO 060042, Romania, and the Institute of Mathematical Statistic and Applied Mathematics, Romanian Academy, Bucharest, Romania (phone: 0040-21-4029153; fax: 004-21-3181016; e-mail: amm@iem.pub.ro).

M. Morega is with the Faculty of Electrical Engineering at the University POLITEHNICA of Bucharest, Bucharest, CO 060042, Romania (e-mail: mihaela@iem.pub.ro).

impact on the atherosclerosis evolution is due to the action of hemodynamic shear stresses on the vascular endothelium. Several studies have shown that the artery morphology (geometry, bifurcations) plays an important role in blood flow and arterial wall shear stress [3].

An outstanding increasing acceptance of numerical simulation is noticed to grow as an advanced research tool in the study of hemodynamic phenomena associated to the cardiovascular flow [2]. Major efforts are devoted to developing methods and means to understand the underlying blood flow hemodynamic and the associated mass transfer processes. The complex geometry of the blood flow circuitry, the vessel wall structure and dynamics due to the cardiac and respiratory motion of the heart influence the coronary hemodynamic [5, 6]. Therefore numerical flow simulations should be conducted in anatomically realistic computational domains. Several simulated arterial geometries under more or less realistic assumptions and different numerical schemes have been employed to perform hemodynamic analysis under either steady or pulsatile flow conditions, on several anatomically idealized models [6, 7].

This work is a continuation of [7]. We are concerned with the numerical simulation analysis of the blood flow in arterial bifurcations and the pressure induced deformation of the wall vessel embedded in the cardiac muscular body. The computational domains are obtained directly out of available medical data, by image reconstruction with the software package Simpleware [8]. The geometry generated in this environment is exported as a finite element (FEM) computational domain in COMSOL Multiphysics environment [9]. The hydrodynamic problem of the artery flow is governed by the momentum and mass conservation laws, and is solved by FEM Galerkin technique, implemented in the software package COMSOL Multiphysics. In the referred study [7], a section of the aortic tree, including bifurcations, is modeled as a solid wall three dimensional domain, while in the analysis presented here, the blood vessels, with elastic walls, are embedded in cardiac

muscle tissue. This structure allows for considering the mechanical interaction between the elastic arterial wall and the flowing blood, leading to the deformation of the artery's internal surface. Fluid dynamics analysis (velocity field and variable pressure distribution) is coupled with the mechanical analysis of the deformation of artery walls.

This study is helpful in planning and optimizing magnetically targeted drug therapies aimed at tumoral abscission. With the help of patient specific, medical image reconstructed geometries of the regions of interest and the interaction between a stationary magnetic field source and biocompatible coated superparamagnetic nanoparticles, numerical models can be built in order to efficiently localize the medical substances therapeutic action, while substantially reducing the unwanted side-effects.

2. THE IMAGE-BASED RECONSTRUCTION PROCESS

Numerical simulations are one of the most important processes in any modern design and research field. Realistic 3D models are essential in obtaining realistic results, and our numerical simulations bring this advantage. The solid models of the blood vessels and those of the surrounding tissue were generated using image-based reconstruction techniques, implemented in Simpleware 4.0 [8].

A. Medical Image Data Import

The first step in any image reconstruction consists of importing the image dataset. In this case, we used ScanIP to import a set of MRI images, stored in DICOM (Digital Imaging and Communication in Medicine) format (Fig. 1).

B. The Segmentation Procedure

The segmentation procedure outlines the regions of interest, and consists of "extracting" of arteries out of the image dataset. First, the *FloodFill Filter* of ScanIP [8] was applied to contour out the blood domain and the arterial walls (Fig. 1). The numerical simulation reported next required the reconstruction of three different domains: the arteries, the blood, and the surrounding muscular mass. The *Erode Filter*, one of the *Morphological Filters* in ScanIP, was used to generate the blood vessels walls.

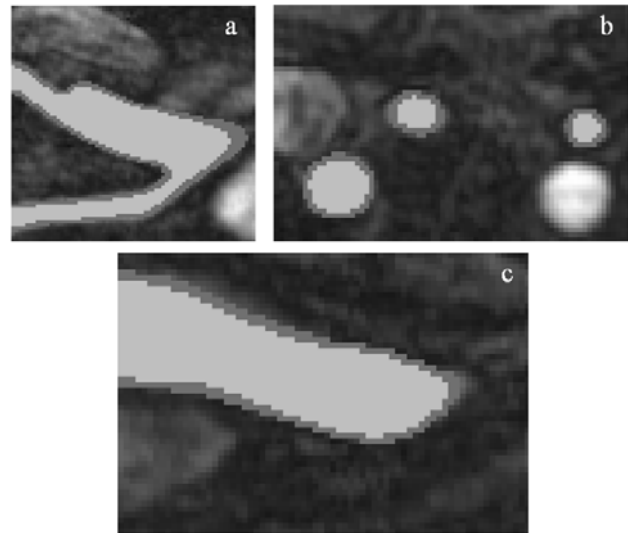


Figure 1: The arteries' walls and the blood domains segmented out of XoY (a), XoZ (b) and ZoY (c) 2D MRI slices.

Fig. 1 shows the result obtained after applying *Invert* and *Subtract* boolean operations. The vessel wall results by inverting the adjusted arteries' mask.

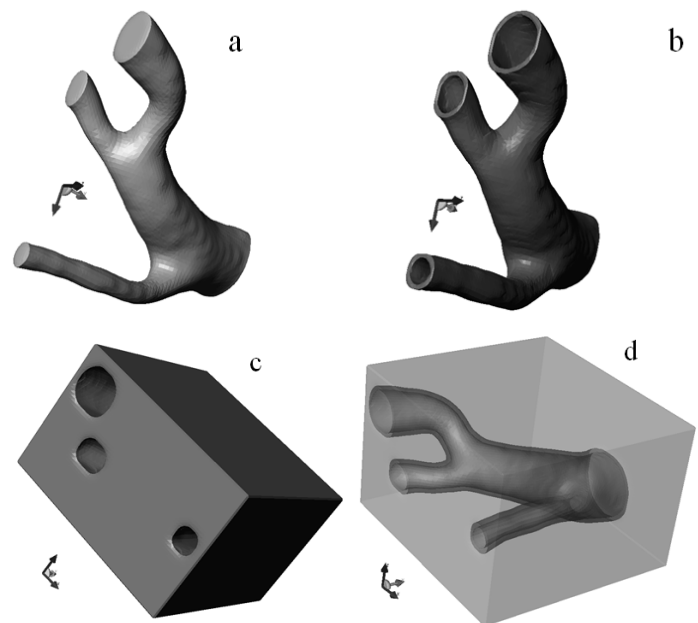


Figure 2: The final 3D solid models of blood (a), arteries (b) and surrounding tissue (c), comprising the whole computational domain (d).

After postprocessing (crop, smooth, resample), all three domains are ready to be meshed, Fig. 2.

C. The FEM Mesh

The solid volumes are then meshed (ScanIP) and exported to Comsol Multiphysics FEM package for numerical modeling and simulation that we used to solve for the fluid-structure interaction, Fig. 3.

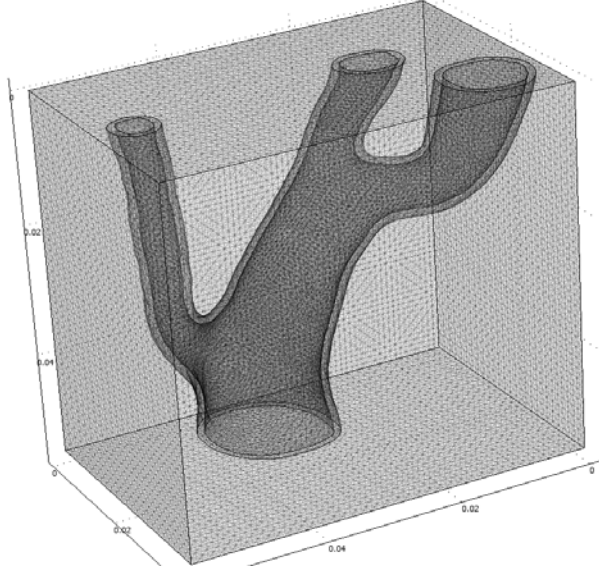


Figure 3: The FEM mesh made of approx. 470,000 tetrahedral, quadratic Lagrange elements.

3. THE MATHEMATICAL MODEL

The analysis accounts for the mechanical response of the cardiac muscle and the vessel walls to the action of the blood flow. The vessels walls are made of elastic fibers that allow them to expand when blood is ejected into them from the heart, and to constrict as blood flows out of them. The cardiac muscle presents stiffness that resists to the artery deformation under the pressure exerted by the blood stream.

The mathematical model that we used couples the hemodynamic to the structural model of the vessel wall and muscular mass where the arterial system is embedded [10].

3.1. The Blood Flow

The fluid (blood) is Newtonian, with constant properties [15]. Its flow is assumed laminar, incompressible, described by the momentum (Navier-Stokes) and mass conservation (\mathbf{u} is the velocity field, p is pressure, ρ is mass density, η is dynamic viscosity, and \mathbf{I} the unit matrix)

$$\rho \left[\frac{\partial \mathbf{u}}{\partial t} + (\mathbf{u} \cdot \nabla) \mathbf{u} \right] = -\nabla \left[-p \mathbf{I} + \eta (\nabla \mathbf{u} + (\nabla \mathbf{u})^T) \right], \quad (1)$$

$$\nabla \cdot \mathbf{u} = 0. \quad (2)$$

The dynamics of the flow – hence, the vessels expansion and constriction under the flow pressure field – is related to the cardiac cycle [6]. The boundary conditions (BC) that close the flow model are as follows: for the blood flow, no-slip velocity conditions at the walls; the inlet and outlet cross sections to the

vessels have prescribed pressure conditions. The arterial structure modeled here belongs to the group of arteries that are known as *resistance vessels* [6]. These vessels have relatively large cross sections, and they oppose little resistance to the flow of blood. Hence the pressure drop is small. In what follows we conjecture that the pressures at the inlet and outlet flow ports of the model vary synchronously.

3.2. The Structural Model

The muscle and artery walls materials are almost incompressible, whereas they can undergo very large strains (finite deformations), and the stress-strain relationship is generally nonlinear. Finite deformations are an adequate assumption when significant rigid-body rotations occur, the strains are no longer small (larger than a few percent), and the loading of the body depends on the deformation [9]. Therefore we assume a hyperelastic law for the artery wall and cardiac muscle, where the large displacement and the constitutive behavior of the materials imply a highly nonlinear behavior [10]. The constitutive law is defined based on a strain energy density function, W . The stresses, S , are computed by deriving W with respect to Green-strains, E , so that $S = \partial W / \partial E$. The strain energy density model used here is neo-Hookean (isotropic model) [10],

$$\bar{W} = \frac{1}{2} J^{-\frac{2}{3}} \left(I - \frac{1}{3} \bar{I}_1 C^{-1} \right) + \frac{1}{2} \kappa J (J - 1) C^{-1}, \quad (3)$$

where $J = \det(\mathbf{F})$ is the ratio between the current and the original volume; \mathbf{F} is the deformation gradient; $\mathbf{C} = \mathbf{F}^T \mathbf{F}$ is the right Cauchy-Green tensor; $I_1 = \text{trace}(\mathbf{C})$; $\bar{I}_1 = I_1 J^{-2/3}$.

The mathematical model was implemented in Comsol Multiphysics [9]. In view of the hyperelastic structural model the vessels and the muscular mass are deformed (expansion and constriction) under the flow field pressure. Therefore the solution strategy is made of two steps: first, the flow part of the problem is solved for; next, using the pressure exerted by the flow on the vessel walls, the structural model is solved for. The dynamic flow is solved for a long enough time until quasisteady periodic regime is obtained (as indicated, e.g., by the wall friction function). Then the flow solution is saved for the following period, for specified time moments. So far the vessels were assumed non-deformable. The structural problem is next solved for using the flow solution (e.g. the pressure field) thus saved.

TABLE 1: MATERIAL PROPERTIES USED IN THE NUMERICAL SIMULATIONS [10]

| Material | Property | Value |
|--|-----------------------|--------------------------|
| Blood | ρ_B | 1060 kg/m ³ |
| | μ_B | 5 m·N·s/m ² |
| Artery wall (neo-Hookean hyperelastic) | ρ_A | 960 kg/m ³ |
| | μ | 6204106 N/m ² |
| | ν (Poisson ratio) | 0.45 |
| Cardiac muscle (neo-Hookean hyperelastic) | ρ_C | 1200 kg/m ³ |
| | μ | 719676 N/m ² |
| | ν (Poisson ratio) | 0.45 |

4. NUMERICAL SIMULATION RESULTS

The one-way coupling between the two models (flow and structure) provides for a more convenient computational load too. The pressure conditions that drive the flow are time dependent, oscillating about the stationary values [6]: $p_2 = 13,290 p_i(t)$ N/m²; $p_3 = 13,040 p_i(t)$ N/m²; $p_1 = 13,300 \cdot p_i(t)$ N/m²; $p_4 = 13,040 p_i(t)$ N/m², $p_i(t) = 1 + K \sin(t + 3/2)$, where K is a factor of order 10^{-1} .

The BC that close the structural model are of displacement type: the faces of the muscular volume are fixed (no displacement), except for the face that contains the inlet of the arterial system (although free, it is not allowed to move in O_y direction) and the face that comprises the exits, which are set free (Fig. 4).

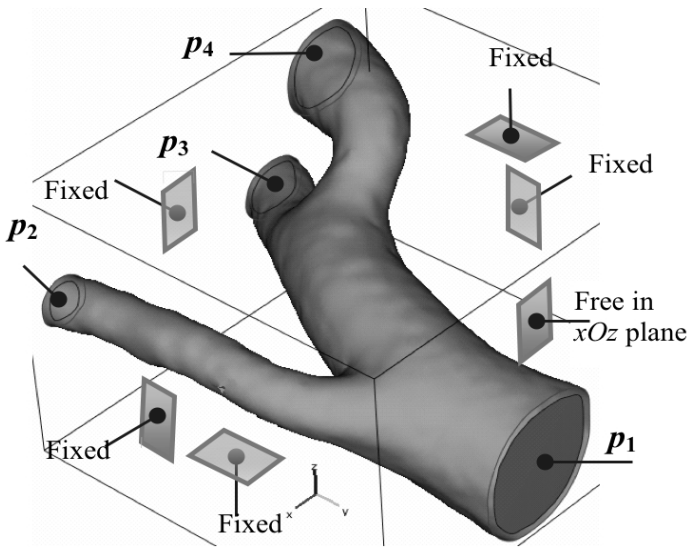
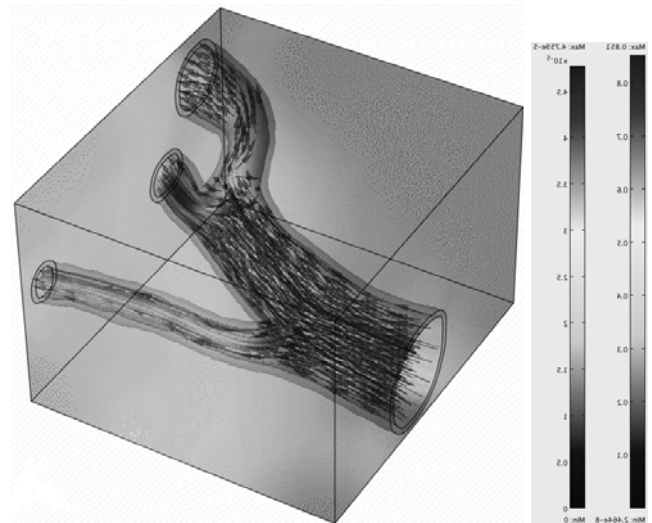
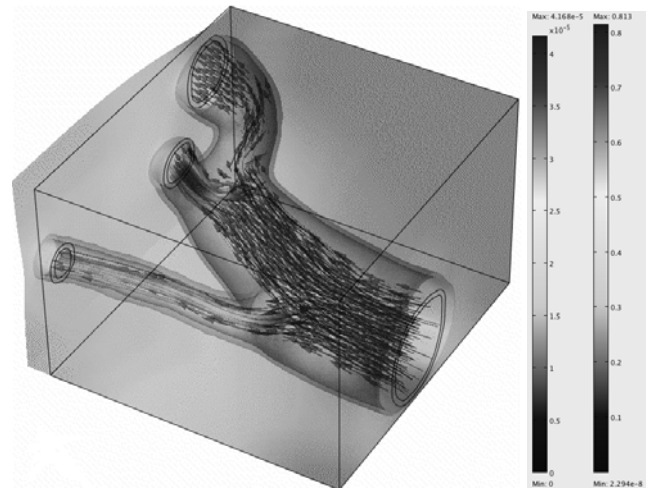


Figure 4: Computational domain and boundary conditions.

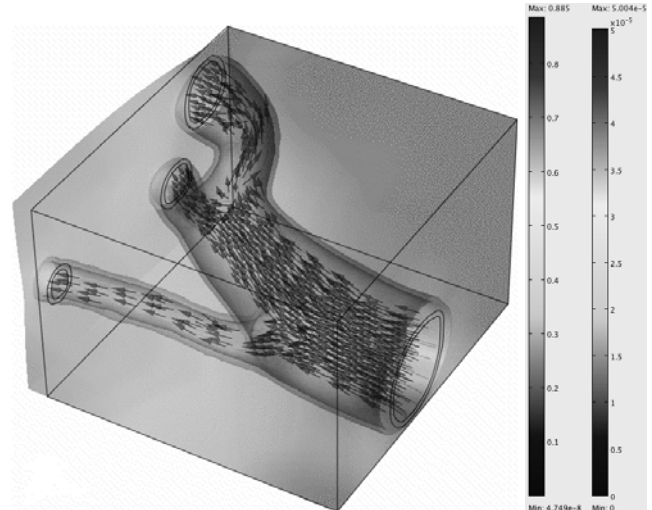
The structural model is solved for steady states, using a parametric solver that reads the pressure field at different moments, produced by the fluid dynamics analysis and previously stored on disk. The solvers utilize the BICGStab algorithm with geometric multigrid preconditioning [9].



a. $t = 0.75$ s



b. $t = 1$ s



c. $t = 1.5$ s

Figure 5: Flow-structure interactions by numerical simulation – deformations are amplified by a factor of 122.

Fig. 5 presents the flow field (arrows and streamlines (tubes), and the deformation of the muscular volume

and vessels walls under the pressure of the flow. The model outlines the influence of large displacements and for the hyperelastic behavior of the biological tissues. Fig. 5,c shows the total displacement at the peak load (after 1.5 s). The displacements are of the order of 10 μm , sustaining the validity of the one-way coupling.

5. CONCLUSIONS

This work is concerned with the blood flow interaction with the arterial vessels and the cardiac muscle, under pulsatile flow conditions. The computational domain was built by image reconstruction. The mathematical model accounts for the nonlinear constitutive behavior of the vessels, muscular mass and the hemodynamic – structural interaction in a one-way coupling: it is only the flow that acts upon the vessels and muscular mass.

The specific morphology and details of the vessels, the flow parameters and the constraints imposed to muscular mass play key roles in the hemodynamic-structural interaction processes. Mass transport patterns and their link with atherosclerosis may be obtained by this approach. This study makes the object of future research.

REFERENCES

- [1] World Health Organization, *Prevention of Cardiovascular Disease. Guidelines for assessment and management of cardiovascular risk*, WHO Press, ISBN 978-92-4-154717-8, 2007.
- [2] BSEC grant, *New cardiovascular planning and diagnostic tool for coronary arteries in BSEC countries using computational simulation*, 2009.
- [3] Broboană, D., Bălan, C., Morega, A. M., Bălan, C., Gheorghe, C., Iacob, R., "Modeling the vortical structures in hemodynamics of small vessels and capillaries," in *Proc. 15th International Congress on Rheology/80th Annual Meeting of the Society-of-Rheology*, Monterey, Ca, USA, August 2008, pp. 03-08.
- [4] Taylor, C. A., Hughes, T. J. R., Zarnis, C. K., "Finite element modeling of 3-Dimensional pulsatile flow in abdominal aorta: relevance to atherosclerosis," *Annals of Biomedical Engineering*, 1998, 26(6), pp. 1-14.
- [5] Zeng, D., Zhaohua, D., Morton, H., Friedman, M. H., Ross Ethier, C., "Effects of Cardiac Motion on Right Coronary Artery Hemodynamic," *Annals of Biomedical Engineering*, 2003, 31, pp. 420–429.
- [6] Feijóo, R. A., *Computational methods in biology*, 2nd Summer School LNCC/MCT, Petrópolis, January 2000.
- [7] Morega, A. M., Dobre, A., Morega, M., Mocanu, D., "Computational Modeling of Arterial Blood Flow," in *Proc. Intl. Conf. on Advancements of Medicine and Health Care through Technology*, Cluj-Napoca, Romania, September 2009, ISSN: 1680-0737, in *Springer Series: IFMBE Proceedings*, vol. 26, pp. 373-378, 2010, ISBN: 978-3-642-04291-1.
- [8] ***Simpleware Ltd., Rennes Drive, Exeter, EX4 4RN, UK, 2009.
- [9] ***COMSOL Multiphysics, v. 3.5a, 2009.
- [10] Bangash, M. Y. H., Bangash, F. N., Bangash Trauma T., "An engineering analysis with medical case studies investigation," Springer, ISBN 3-540-36305-X, 2007.

Computer Simulation of Plaque formation and Development

Filipovic, D., Nenad; Meunier, Nicolas; Kojic, Milos; Isailovic, Velibor; Radovic, Milos; Milosevic, Zarko; Nikolic, Dalibor; Milasinovic, Danko; Exarchos, Themis; Parodi, Oberdan; and Fotiadis, Dimitris

Abstract—*Atherosclerosis develops from oxidized low-density lipoprotein molecules (LDL). When oxidized LDL evolves in plaque formations within an artery wall, a series of reactions occur to repair the damage to the artery wall caused by oxidized LDL. The body's immune system responds to the damage to the artery wall caused by oxidized LDL by sending specialized white blood cells-macrophages (Mphs) to absorb the oxidized-LDL forming specialized foam cells. Macrophages accumulate inside arterial intima. Also Smooth Muscle Cells (SMC) accumulate in the atherosclerotic arterial intima, where they proliferate and secrete extracellular matrix to form a fibrous cap.*

In this study, we simulate a process of atherosclerosis formation and development and compare it with literature data. The 3D blood flow is governed by the Navier-Stokes equations, together with the continuity equation. Mass transfer within the blood lumen and through the arterial wall is coupled with the blood flow and is modeled by the convection-diffusion equation. LDL transport in lumen of the vessel is described by Kedem-Katchalsky equations. The inflammatory process is solved using three additional reaction-diffusion partial differential equations.

The understanding and the prediction of the evolution of atherosclerotic plaques either into vulnerable plaques or into stable plaques are major tasks for the medical community.

Manuscript received March 1, 2011. This work was supported by European Commission (Project ARTREAT, ICT 224297).

N. D. Filipović, is with the Faculty of Mechanical Engineering, Kragujevac, Serbia (e-mail: fica@kg.ac.rs).

N. Meunier is with Paris Descartes University (Paris V), Paris, FRANCE, (e-mail: nicolas.meunier@math-info.univ-paris5.fr)

M. Kojic is with Bioengineering Research and Development Center, BioIRC, Kragujevac, Serbia, Harvard School of Public Health and Department of Nanomedicine and Biomedical Engineering, University of Texas Medical Center at Houston (e-mail: mkojic@hsph.harvard.edu)

V. Isailovic, M. Radovic, Z. Milosevic, D. Nikolic and D. Milasinovic are with the Research and Development Center for Bioengineering "BioIRC", Kragujevac, Serbia (phone: 381-34-301920; fax: 381-34-500089; e-mail: velibor@kg.ac.rs, mradovic@kg.ac.rs, zarko@kg.ac.rs, markovac85@kg.ac.rs, dmilashinovic@kg.ac.rs).

T. Exarchos and D. Fotiadis are with the Foundation of Research and Technology Hellas - Biomedical Research Institute, Ioannina, Greece and with the Unit of Medical Technology and Intelligent Information Systems, Dept of Material Science and Engineering, University of Ioannina, Ioannina, Greece. (email: exarchos@cc.uoi.gr, fotiadis@cc.uoi.gr)

O. Parodi is with the Istituto di Fisiologia Clinica, Consiglio Nazionale delle Ricerche, Pisa, Italy (email: oberpar@tin.it)

Index Terms — Atherosclerosis, Computer simulation, Plaque formation.

1. INTRODUCTION

ATHEROSCLEROSIS is a progressive disease characterized in particular by the accumulation of lipids and fibrous elements in artery walls. Over the past decade, scientists come to appreciate a prominent role for inflammation in atherosclerosis.

Atherosclerosis is characterized by dysfunction of endothelium, vasculitis and accumulation of lipid, cholesterol and cell elements inside blood vessel wall. This process develops in arterial walls. Atherosclerosis develops from oxidized low-density lipoprotein molecules (LDL). When oxidized LDL evolves in plaque formations within an artery wall, a series of reactions occur to repair the damage to the artery wall caused by oxidized LDL. The body's immune system responds to the damage to the artery wall caused by oxidized LDL by sending specialized white blood cells-macrophages (Mphs) to absorb the oxidized-LDL forming specialized foam cells. Macrophages accumulate inside arterial intima. Also Smooth Muscle Cells (SMC) accumulate in the atherosclerotic arterial intima, where they proliferate and secrete extracellular matrix to form a fibrous cap [1]. Unfortunately, macrophages are not able to process the oxidized-LDL, and ultimately grow and rupture, depositing a larger amount of oxidized cholesterol into the artery wall. The atherosclerosis process is shown in Fig. 1.

This chapter describes a completely new computer model for plaque formation and development. The first section is devoted to the LDL model of transport from the lumen to intima and detailed three-dimensional model for inflammatory and plaque progression process. The next section describes some of the benchmark examples for 2D, 2D axi-symmetric and 3D model of plaque formation and development. At the end a complex specific-patient 3D model is given. Finally the main conclusions of the work are addressed.

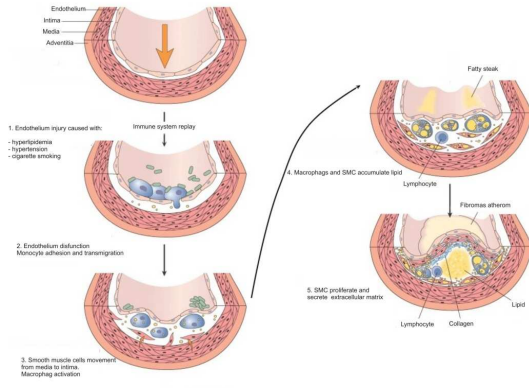


Figure 1: Atherosclerotic plaque development (adapted from [1])

2. METHODS

In this section a continuum based approach for plaque formation and development in three-dimension is presented. All algorithms are incorporated in program PAK-Athero from University of Kragujevac [2].

2.1 Governing equations for modeling of LDL transport through the arterial wall

The governing equations and numerical procedures are given. The blood flow is simulated by the three-dimensional Navier-Stokes equations, together with the continuity equation

$$-\mu \nabla^2 \mathbf{u}_l + \rho (\mathbf{u}_l \cdot \nabla) \mathbf{u}_l + \nabla p_l = 0 \quad \text{Eq. (1)}$$

$$\nabla \cdot \mathbf{u}_l = 0 \quad \text{Eq. (2)}$$

where \mathbf{u}_l is blood velocity in the lumen, p_l is the pressure, μ is the dynamic viscosity of the blood, and ρ is the density of the blood.

Mass transfer in the blood lumen is coupled with the blood flow and modelled by the convection-diffusion equation as follows

$$\nabla \cdot (-D_l \nabla c_l + c_l \mathbf{u}_l) = 0 \quad \text{Eq. (3)}$$

in the fluid domain, where c_l is the solute concentration in the blood lumen, and D_l is the solute diffusivity in the lumen.

Mass transfer in the arterial wall is coupled with the transmural flow and modelled by the convection-diffusion-reaction equation as follows

$$\nabla \cdot (-D_w \nabla c_w + c_w \mathbf{u}_w) = r_w c_w \quad \text{Eq. (4)}$$

in the wall domain, where c_w is the solute concentration in the arterial wall, D_w is the solute diffusivity in the arterial wall, K is the solute lag coefficient, and r_w is the consumption rate constant.

LDL transport in lumen of the vessel is coupled with Kedem-Katchalsky equations:

$$J_v = L_p (\Delta p - \sigma_d \Delta \pi) \quad \text{Eq. (5)}$$

$$J_s = P \Delta c + (1 - \sigma_f) J_v \bar{c} \quad \text{Eq. (6)}$$

where L_p is the hydraulic conductivity of the endothelium, Δc is the solute concentration difference across the endothelium, Δp is the pressure drop across the endothelium, $\Delta \pi$ is the oncotic pressure difference across the

endothelium, σ_d is the osmotic reflection coefficient, σ_f is the solvent reflection coefficient, P is the solute endothelial permeability, and \bar{c} is the mean endothelial concentration.

The basic relations for mass transport in the artery. The metabolism of the artery wall is critically dependent upon its nutrient supply governed by transport processes within the blood. A two different mass transport processes in large arteries are addressed. One of them is the oxygen transport and the other is LDL transport. Blood flow through the arteries is usually described as motion of a fluid-type continuum, with the wall surfaces treated as impermeable (hard) boundaries. However, transport of gases (e.g. O_2 , CO_2) or macromolecules (albumin, globulin, LDL) represents a convection-diffusion physical process with permeable boundaries through which the diffusion occurs. In the analysis presented further, the assumption is that the concentration of the transported matter does not affect the blood flow (i.e. a diluted mixture is considered). The mass transport process is governed by convection-diffusion equation,

$$\frac{\partial c}{\partial t} + v_x \frac{\partial c}{\partial x} + v_y \frac{\partial c}{\partial y} + v_z \frac{\partial c}{\partial z} = D \left(\frac{\partial^2 c}{\partial x^2} + \frac{\partial^2 c}{\partial y^2} + \frac{\partial^2 c}{\partial z^2} \right) \quad \text{Eq. (7)}$$

where c denotes the macromolecule or gas concentration; v_x , v_y and v_z are the blood velocity components in the coordinate system x, y, z , and D is the diffusion coefficient, assumed constant, of the transported material.

Boundary conditions for transport of the LDL. A macromolecule directly responsible for the process of atherosclerosis is LDL which is well known as atherogenic molecule. It is also known that LDL can go through the endothelium at least by three different mechanisms, namely, receptor-mediated endocytosis, pinocytotic vesicular transport, and phagocytosis [3]. The permeability coefficient of an intact arterial wall to LDL has been reported to be of the order of 10^{-8} [cm/s] [4]. The conversion of the mass among the LDL passing through a semipermeable wall, moving toward the vessel wall by a filtration flow and diffusing back to the mainstream at the vessel wall, is described by the relation

$$c_w v_w - D \frac{\partial c}{\partial n} = K c_w \quad \text{Eq. (8)}$$

where c_w is the surface concentration of LDL, v_w is the filtration velocity of LDL transport through the wall, n is coordinate normal to the wall, D is the diffusivity of LDL, and K is the overall mass transfer coefficient of LDL at the vessel wall. A uniform constant concentration C_0 of LDL is applied at the artery tree inlet as classical inlet boundary condition for eq. (7).

2.2 Finite Element Modeling of Diffusion-Transport Equations

In the case of blood flow with mass transport we have domination of the convection terms due to the low diffusion coefficient [5]. Then it is

3. RESULTS

3.1 2D Model of Plaque Formation and Development

For the first example of a two-dimensional model of the mild stenosis, a fully developed parabolic steady velocity profile was assumed at the lumen inlet boundary

$$u(r) = 2U_0 \left(1 - \left(\frac{2r}{D} \right)^2 \right) \quad \text{Eq. (15)}$$

where $u(r)$ is the velocity in the axial direction at radial position r ; D is the inlet diameter; and U_0 is the mean inlet velocity. At the lumen side of the endothelial boundary, a lumen-to-wall transmural velocity in the normal direction was specified:

$$\begin{aligned} \mathbf{t}_l^T \cdot \mathbf{u}_l &= 0 \quad \text{Eq. (16)} \\ \mathbf{u}_l \mathbf{n}_l &= \mathbf{J}_v \end{aligned}$$

where \mathbf{t}_l^T and \mathbf{n}_l are the tangential and normal unit vectors of fluid subdomain, respectively. Oxidized LDL distribution for a mild stenosis is shown in Fig. 2.

necessary to employ special stabilizing techniques in order to obtain a stable numerical solution. The streamline upwind/Petrov-Galerkin stabilizing technique (SUPG) [6] within a standard numerical integration scheme is implemented. The incremental-iterative form of finite element equations of balance are obtained by including the diffusion equations and transforming them into incremental form. The final equations are

$$\begin{aligned} & \left[\begin{array}{ccc|c} \frac{1}{\Delta t} \mathbf{M}_c + {}^{n+1} \mathbf{K}_{vv}^{(i-1)} + {}^{n+1} \mathbf{K}_{pv}^{(i-1)} + {}^{n+1} \mathbf{J}_{vv}^{(i-1)} & & & \mathbf{0} \\ & \mathbf{K}_{vp}^T & & \mathbf{0} \\ & & \mathbf{0} & \mathbf{0} \\ & {}^{n+1} \mathbf{K}_{cv}^{(i-1)} & & \frac{1}{\Delta t} \mathbf{M}_c + {}^{n+1} \mathbf{K}_{cc}^{(i-1)} + {}^{n+1} \mathbf{J}_{cc}^{(i-1)} \end{array} \right] \times \\ & \left\{ \begin{array}{l} \Delta \mathbf{V}^{(i)} \\ \Delta \mathbf{P}^{(i)} \\ \Delta \mathbf{C}^{(i)} \end{array} \right\} = \left\{ \begin{array}{l} {}^{n+1} \mathbf{F}_v^{(i-1)} \\ {}^{n+1} \mathbf{F}_p^{(i-1)} \\ {}^{n+1} \mathbf{F}_c^{(i-1)} \end{array} \right\} \end{aligned} \quad \text{Eq. (9)}$$

where the matrices are

$$\begin{aligned} (\mathbf{M}_c)_{\beta\beta k} &= \int \rho N_k N_j dV, & (\mathbf{M}_c)_{\beta\beta k} &= \int N_k N_j dV \\ ({}^{n+1} \mathbf{K}_{cc}^{(i-1)})_{\beta\beta k} &= \int DN_{k,j} N_j dV, & ({}^{n+1} \mathbf{K}_{pv}^{(i-1)})_{\beta\beta k} &= \int \mu N_{k,j} N_j dV \\ ({}^{n+1} \mathbf{K}_{cv}^{(i-1)})_{\beta\beta k} &= \int N_k {}^{n+1} c_j^{(i-1)} N_j dV, & ({}^{n+1} \mathbf{K}_{vv}^{(i-1)})_{\beta\beta k} &= \int \rho N_k {}^{n+1} v_j^{(i-1)} N_j dV \\ ({}^{n+1} \mathbf{J}_{cc}^{(i-1)})_{\beta\beta k} &= \int \rho N_k {}^{n+1} v_j^{(i-1)} N_j dV, & ({}^{n+1} \mathbf{K}_{vp}^{(i-1)})_{\beta\beta k} &= \int \rho N_k \hat{N}_j dV \\ ({}^{n+1} \mathbf{J}_{vv}^{(i-1)})_{\beta\beta k} &= \int \rho N_k {}^{n+1} v_j N_j dV \end{aligned} \quad \text{Eq. (10)}$$

and the vectors are

$$\begin{aligned} {}^{n+1} \mathbf{F}_c^{(i-1)} &= {}^{n+1} \mathbf{F}_q + {}^{n+1} \mathbf{F}_{ac}^{(i-1)} - \frac{1}{\Delta t} \mathbf{M}_c \{ {}^{n+1} \mathbf{C}^{(i-1)} - {}^n \mathbf{C} \} - \\ & \quad {}^{n+1} \mathbf{K}_{cv}^{(i-1)} \{ {}^{n+1} \mathbf{V}^{(i-1)} \} - {}^{n+1} \mathbf{K}_{cc}^{(i-1)} \{ {}^{n+1} \mathbf{C}^{(i-1)} \} \\ ({}^{n+1} \mathbf{F}_q)_k &= \int N_k q^b dV, & ({}^{n+1} \mathbf{F}_{ac}^{(i-1)})_k &= \int DN_k \nabla {}^{n+1} c^{(i-1)} \cdot \mathbf{n} dS \end{aligned} \quad \text{Eq. (11)}$$

Note that \hat{N}_j are the interpolation functions for pressure (which are taken to be for one order of magnitude lower than interpolation functions N_j for velocities). The matrices \mathbf{M}_{cc} and \mathbf{K}_{cc} are the 'mass' and convection matrices; \mathbf{K}_{cv} and \mathbf{J}_{cc} correspond to the convective terms of equation (7); and \mathbf{F}_c is the force vector which follows from the convection-diffusion equation in (7) and linearization of the governing equations.

2.3 Modeling of Plaque Formation and Development

The inflammatory process was solved using three additional reaction-diffusion partial differential equations [7, 8]:

$$\begin{aligned} \partial_t Ox &= d_2 \Delta Ox - k_1 Ox \cdot M \\ \partial_t M + \text{div}(v_w M) &= d_1 \Delta M - k_1 Ox \cdot M + S / (1 - S) \\ \partial_t S &= d_3 \Delta S - \lambda S + k_1 Ox \cdot M + \gamma (Ox - Ox^{thr}) \end{aligned} \quad \text{Eq. (12)}$$

where Ox is the oxidized LDL or c_w - the solute concentration in the wall from eq. (7); M and S are concentrations in the intima of macrophages and cytokines, respectively; d_1, d_2, d_3 are the corresponding diffusion coefficients; λ and γ degradation and LDL oxidized detection coefficients; and v_w is the inflammatory velocity of plaque growth, which satisfies Darcy's law and continuity equation [5, 9, 10, 11]:

$$v_w - \nabla \cdot (\mathbf{p}_w) = 0 \quad \text{Eq. (13)}$$

$$\nabla \cdot \mathbf{v}_w = 0 \quad \text{Eq. (14)}$$

in the wall domain. Here, \mathbf{p}_w is the pressure in the arterial wall.

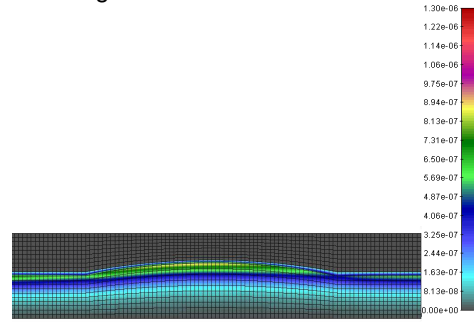


Figure 2: Oxidized LDL distribution for a mild stenosis (30% constriction by area)

3.2 2D axi-symmetric model of plaque formation and development

The plaque formation and development is modeled through an initial straight artery in 2D axi-symmetric model with mild constriction of 30%. The inlet artery diameter $d_0=0.4$ [cm]. Blood was modeled as a Newtonian fluid with density $\rho=1.0$ [g/cm³] and viscosity $\mu=0.0334$ [P]. The steady state conditions for fluid flow and mass transport are assumed. The entering blood velocity is defined by the Reynolds number Re (calculated using the mean blood velocity and the artery diameter).

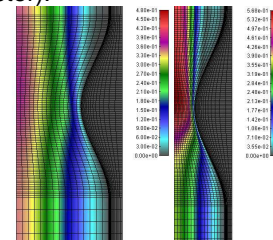


Figure 3: a) Velocity distribution for an initial mild stenosis 30% constriction by area b) Velocity distribution at the end of stenosis process after 10^7 sec [units m/s]

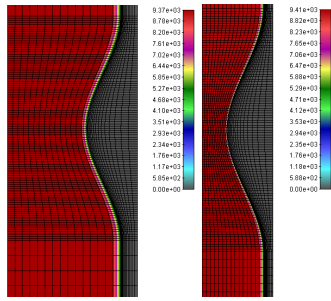


Figure 4: a) Pressure distribution for an initial mild stenosis 30% constriction by area b) Pressure distribution at the end of stenosis process after 10^7 sec[units Pa]

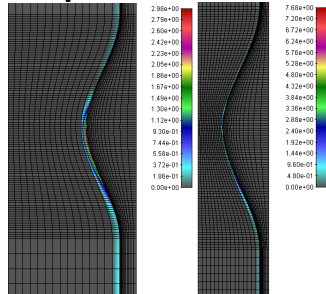


Figure 5: a) Shear stress distribution for an initial mild stenosis 30% constriction by area b) Shear stress distribution at the end of stenosis process after 10^7 sec[units dyn/cm²]

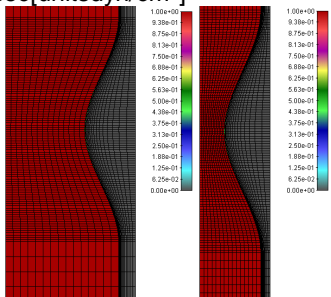


Figure 6: a) Lumen LDL distribution for an initial mild stenosis 30% constriction by area b) Lumen LDL distribution at the end of stenosis process after 10^7 sec[units mg/mL]

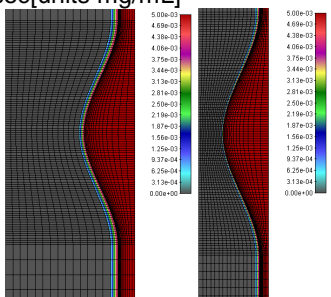


Figure 7: a) Oxidized LDL distribution in the intima for an initial mild stenosis 30% constriction by area b) Oxidized LDL distribution in the intima at the end of stenosis process after 10^7 sec[units mg/mL]

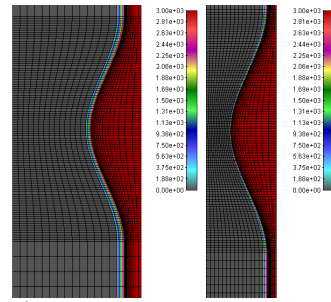


Figure 8: a) Intima wall pressure distribution for an initial mild stenosis 30% constriction by area b) Intima wall pressure distribution at the end of stenosis process after 10^7 sec[units Pa]

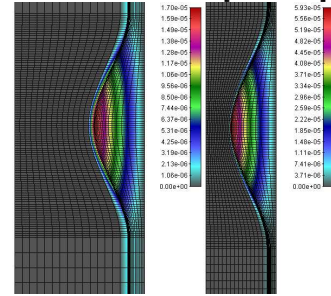


Figure 9: a) Macrophages distribution in the intima for an initial mild stenosis 30% constriction by area b) Macrophages distribution in the intima at the end of stenosis process after 10^7 sec[units mg/mL]

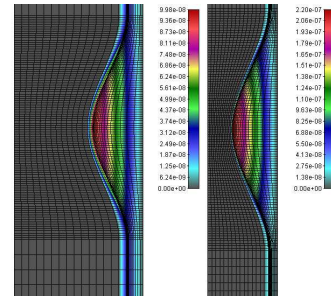


Figure 10: a) Cytokines distribution in the intima for an initial mild stenosis 30% constriction by area b) Cytokines distribution in the intima at the end of stenosis process after 10^7 sec[units mg/mL]

3.3 3D Model of Plaque Formation and Development

In order to make benchmark example for three-dimensional simulation we tested simple middle stenosis with initial 30% constriction for time period of $t=10^7$ sec (approximately 7 years) and compare results with 2D axi-symmetric model. The results for velocity distribution for initial and end stage of simulations are presented in Fig. 11a and Fig. 11b. The pressure and shear stress distributions for start and end time are given in Fig. 12 and Fig. 13. Concentration distribution of LDL inside the lumen domain and oxidized LDL inside the intima are presented in Fig. 14 and Fig. 15. The transmural wall pressure is presented in Fig. 16. Macrophages and cytokines distributions are shown in Fig. 17 and Fig. 18. The diagram of three-dimensional plaque volume growing during time is given in Fig. 19. It can be seen that time period for developing of

stenosis corresponds to data available in the literature [12].

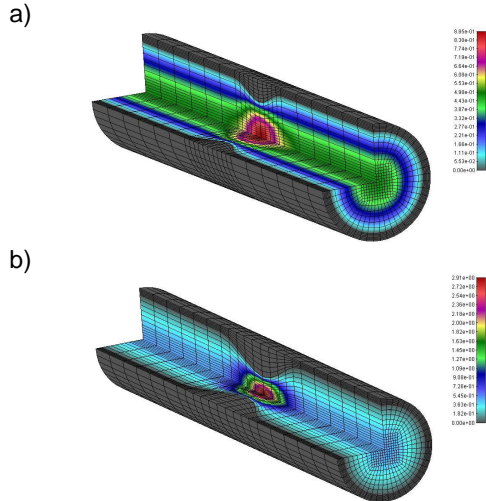


Figure 11: a) Velocity distribution for an initial mild stenosis 30% constriction by area b) Velocity distribution at the end of stenosis process after 10^7 sec[unitsm/s]

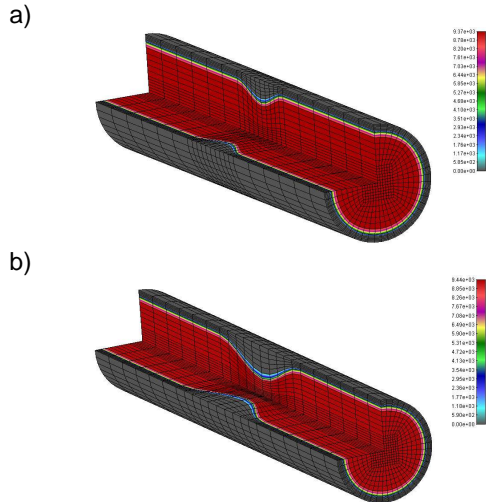


Figure 12: a) Pressure distribution for an initial mild stenosis 30% constriction by area b) Pressure distribution at the end of stenosis process after 10^7 sec[units Pa]

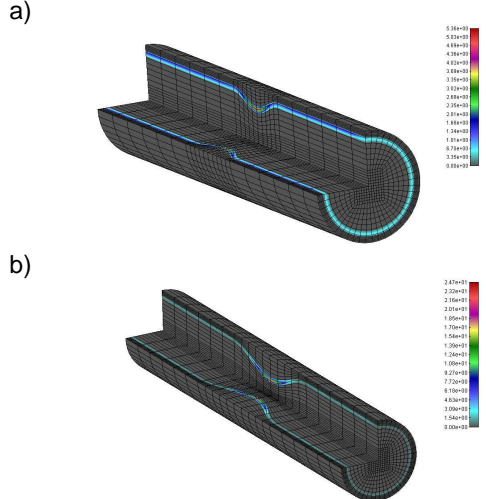


Fig. 13. a) Shear stress distribution for an initial mild stenosis 30% constriction by area b) Shear

stress distribution at the end of stenosis process after 10^7 sec[unitsdyn/cm²]

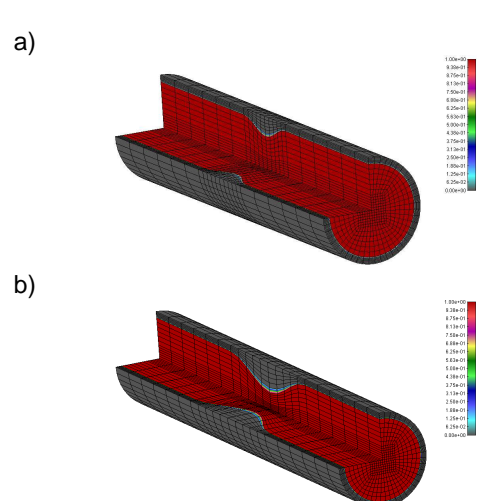


Figure 14: a) Lumen LDL distribution for an initial mild stenosis 30% constriction by area b) Lumen LDL distribution at the end of stenosis process after 10^7 sec[units mg/mL]

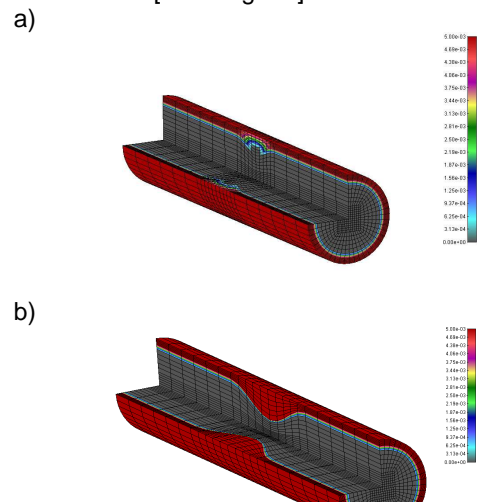


Figure 15: a) Oxidized LDL distribution in the intima for an initial mild stenosis 30% constriction by area b) Oxidized LDL distribution in the intima at the end of stenosis process after 10^7 sec[units mg/mL]

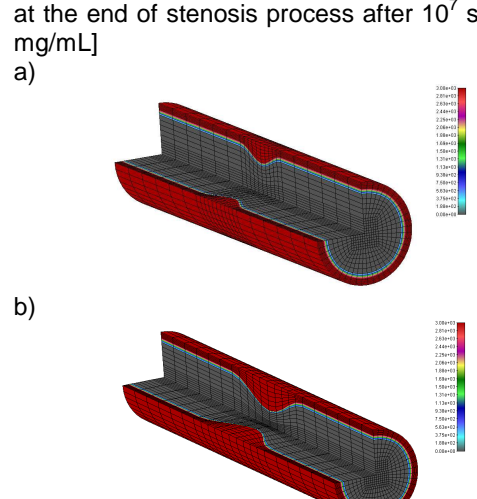
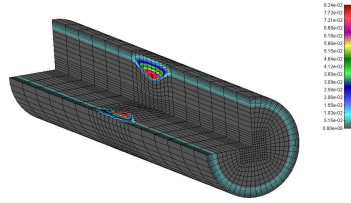


Figure 16: a) Intima wall pressure distribution for an initial mild stenosis 30% constriction by area b)

Intima wall pressure distribution at the end of stenosis process after 10^7 sec[units Pa]
a)



b)

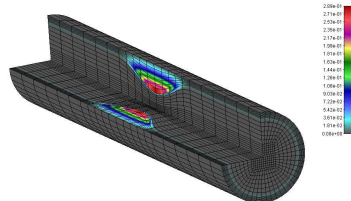
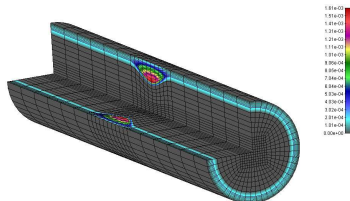


Figure 17: a) Macrophages distribution in the intima for an initial mild stenosis 30% constriction by area b) Macrophages distribution in the intima at the end of stenosis process after 10^7 sec[units mg/mL]

a)



b)

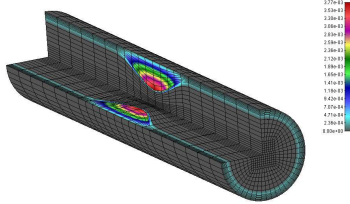


Figure 18: a) Cytokines distribution in the intima for an initial mild stenosis 30% constriction by area b) Cytokines distribution in the intima at the end of stenosis process after 10^7 sec[units mg/mL]

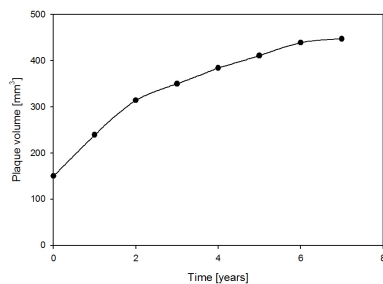


Figure 19: Plaque progression during time (computer simulation)

From above figures it can be observed that during time plaque is progressing and all the variables as velocity distribution, shear stress, macrophages, cytokines are increasing. Also from Fig. 19 it can be seen that plaque progression in volume during time corresponds to clinical findings [13].

The last example is a model of the patient specific Left Anterior Descending(LAD)coronary artery for steady flow conditions. Computed concentration of LDL indicates that there is a newly formed matter in the intima, especially in the flow separation region in the LAD artery (Fig. 20).

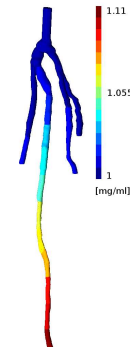


Figure 20: LDL concentration distribution in the left anterior descending coronary artery

4. DISCUSSION AND CONCLUSIONS

Full three-dimensional model was created for plaque formation and development, coupled with blood flow and LDL concentration in blood. The models for plaque initiation and plaque progression are developed. These two models are based on partial differential equations with space and times variables and they describe the biomolecular process that takes place in the intima during the initiation and the progression of the plaque. The model for plaque formation and plaque progression despite some difficulties concerning the different time scales that are involved and the different blood velocities in the lumen and in the intima, its numerical treatment is developed by using decomposition techniques together with finite elements methods and by splitting the numerical scheme into three independent parts: blood flow and LDL transfer, inflammatory process and atheromatous plaque evolution.

Determination of plaque location and progression in time for a specific patient shows a potential benefit for future prediction of this vascular disease using computer simulation. The understanding and the prediction of the evolution of atherosclerotic plaques either into vulnerable plaques or into stable plaques are major tasks for the medical community.

ACKNOWLEDGMENT

This work is part funded by European Commission (Project ARTREAT, ICT 224297).

REFERENCES

- [1] Loscalzo, J., Schafer, A. I., "Thrombosis and Hemorrhage," Third edition, Lippincott Williams & Wilkins, 978-0781730662, Philadelphia, 2003.
- [2] Filipovic, N., Meunier, N., Kojic, M., "PAK-Athero, Specialized three-dimensional PDE software for simulation of plaque formation and development inside the arteries," University of Kragujevac, 34000 Kragujevac, Serbia, 2010.
- [3] Goldstein, J., Anderson, R., Brown, M., "Coated pits, coated vesicles, and receptor-mediated endocytosis," Nature, 1979, 279, pp. 679-684.

- [4] Bratzler, R. L., Chisolm, G.M., Colton, C. K., Smith, K. A., Lees, R.S., "The distribution of labeled low-density lipoproteins across the rabbit thoracic aorta in vivo," *Atherosclerosis*, 1977, 28(3), pp. 289–307.
- [5] Kojic, M., Filipovic, N., Stojanovic, B., Kojic, N., "Computer Modeling in Bioengineering – Theoretical Background, Examples and Software," John Wiley and Sons, 978-0-470-06035-3, England. 2008.
- [6] Brooks, A. N., Hughes, T. J. R., "Streamline upwind/Petrov-Galerkin formulations for convection dominated flows with particular emphasis on the incompressible Navier-Stokes equations," *Comput. Meths. Appl. Mech. Engrg.*, 1982, 32(1-3), pp. 199-259.
- [7] Calvez, V., Ebde, A., Meunier, N., Raoult, A., "Mathematical modelling of the atherosclerotic plaque formation," *Proceedings of ESAIM*, 2008, 28, pp. 1-12.
- [8] Boynard, M., Calvez, V., Hamraoui, A., Meunier, N., Raoult, A., "Mathematical modelling of earliest stage of atherosclerosis," *Proceedings of COMPDYN 2009 - SEECM 2009*, Rhodes, 2009.
- [9] Filipovic, N., Kojic, M., "Computer simulations of blood flow with mass transport through the carotid artery bifurcation," *Theoret. Appl. Mech. (Serbian)*, 2004, 31(1), pp. 1-33.
- [10] Filipovic, N., Mijailovic, S., Tsuda, A., Kojic, M., "An Implicit Algorithm Within The Arbitrary Lagrangian-Eulerian Formulation for Solving Incompressible Fluid Flow With Large Boundary Motions," *Comp. Meth. Appl. Mech. Eng.*, 2006a, 195(44-47), pp. 6347-6361.
- [11] Filipovic, N., Kojic, M., Ivanovic, M., Stojanovic, B., Otasevic, L., Rankovic, V., "MedCFD, Specialized CFD software for simulation of blood flow through arteries," University of Kragujevac, 34000 Kragujevac, Serbia, 2006b.
- [12] Goh, V. K., Lau, C. P., Mohlenkamp, S., Rumberger, J. A., Achenbach A., Budoff, M. J., "Outcome of coronary plaque burden: a 10-year follow-up of aggressive medical management," *Cardiovascular Ultrasound*, 2010, 8:5.
- [13] Verstraete, M., Fuster, V., Topol, E. J., "Cardiovascular Thrombosis: Thrombocardiology and Thromboneurology," Second Edition, Lippincot-Raven Publishers, 978-0397587728, Philadelphia, 1998.
- [14] Caro, C. G., Fitz-Gerald, J. M., Schroter, R. C., "Atheroma and Arterial Wall Shear. Observation, Correlation and Proposal of a Shear Dependent Mass Transfer Mechanism for Atherogenesis," *Proc. R. Soc. London*, 1971, 177(46), pp. 109–159.

ARTool: A Platform for the Development of Multi-level patient-specific artery and atherogenesis models

Exarchos, P., Themis; Stefanou, Kostas; Siogkas, K., Panagiotis; Sakelarios, Antonis; Fotiadis, I., Dimitrios; Naka, Katerina; Michalis, Lampros; Filipovic, Nenad; Parodi, Oberdan

Abstract - This work describes a platform used for the visualization and modelling of biological processes during the formation and development of atheroma, called ARTool. Atherosclerotic lesions can be visualized via imaging modalities like Computed Tomography (CT), Magnetic Resonance Imaging (MRI) as well as Intravascular Ultrasound (IVUS) and Angiography. The produced medical images are then processed by ARTool, generating accurate patient – specific 3 – D reconstructed arterial models. The arterial model is used to study blood flow dynamics, mass transfer and plaque growth. Due to the fact that ARTool is able to process all modalities simultaneously and perform the required calculations in parallel, results are generated almost in real time.

Index Terms—3D image reconstruction, Atherosclerosis, Blood flow dynamics

1. INTRODUCTION

Atherosclerosis is the most prevalent cardiovascular disease causing the death of millions of people annually. Atherosclerosis is a vascular disease associated with the accumulation of lipids which results to the invasion of leukocytes and smooth muscle cells into the intima. This biological process may lead to the formation of plaque on the arterial wall resulting to arterial wall hardening. The development of plaque is a process influenced by mechanical, biochemical and biological factors. Initial attempts to understand the complexity of this process consisted of *in vitro* experiments. The process of the atherosclerotic plaque formation was then modelled with newly

Manuscript received December 21, 2010 This work was part funded by the EC (Project ARTreat: Multi-level patient-specific artery and atherogenesis model for outcome prediction, decision support treatment, and virtual hand-on training, FP7 – 224297)

T. Exarchos, K. Stefanou, A. Sakelarios, P. Siogkas and D. Fotiadis are with the Foundation of Research and Technology Hellas -Biomedical Research Institute, Ioannina, Greece and with the Unit of Medical Technology and Intelligent Information Systems, Dept of Material Science and Engineering, University of Ioannina, Ioannina, Greece. (email: exarchos@cc.uoi.gr, kstefan@cc.uoi.gr, ansakel@cc.uoi.gr, psioiskas@cc.uoi.gr, fotiadis@cc.uoi.gr)

K. Naka and L. Michalis are with the Medical School, University of Ioannina, Ioannina, Greece (email: anaka@cc.uoi.gr, lmichalis@cc.uoi.gr)

N. Filipovic is with the University of Kragujevac, Kragujevac, Serbia (email: fica@kg.ac.rs)

O. Parodi is with the Istituto di Fisiologia Clinica, Consiglio Nazionale delle Ricerche, Pisa, Italy (email: oberpar@tin.it)

developed simulation procedures. Data obtained from several artery imaging modalities, such as Intravascular Ultrasound (IVUS) and Angiography, Magnetic Resonance Imaging (MRI) and Computed Tomography (CT) constitute the basis of arterial modeling. Fusion of IVUS and Angiography images was used for the 3D reconstruction of coronary arteries by Bourantas et al. [1,2], whereas Zifan et al. [3] proposed an automated method for the 3D reconstruction of coronary arteries with the use of monoplane X-ray angiographies. High-resolution MRI was used for the reconstruction of atherosclerotic arteries by Auer et al. [4]. Steinman et al. [5] proposed a reconstruction method applicable to the carotid artery bifurcation from MRI data. The reconstructed 3D models have been employed to simulate blood flow and to examine the effect of shear stress distribution on plaque development. Blood flow affects endothelial function and in turn promotes atherosclerosis. Regions of geometries which create complex flows such as curvatures and bifurcations are more prone to plaque development. Canic et al. [6] performed blood flow simulations in compliant unrealistic arterial models. The Navier – Stokes equations were used to model blood flow whereas the arterial wall was described as linear viscoelastic. In other studies, computational models have been developed directly from image modalities, mainly from MRI [7]. The mechanical properties of the arterial wall have been described with several models, as in [8] where a comparative study on modeling arterial mechanics was presented.

In this work, a powerful processing platform for the 3D reconstruction of coronary and carotid arteries called ARTool is presented using various imaging modalities such as IVUS, Angiography, MRI and CT. The proposed tool incorporates efficient algorithms which enable the clinician to perform blood flow simulations and study flow dynamics as well as predict the regions prone to plaque evolution based on the mass transport in the blood. The architecture, the functionalities and the implementation of the aforementioned system are presented.

2. METHODS

ARTool provides patient specific artery and atherogenesis model in three different levels (Fig. 1): (i) 3D artery reconstruction, (ii) blood

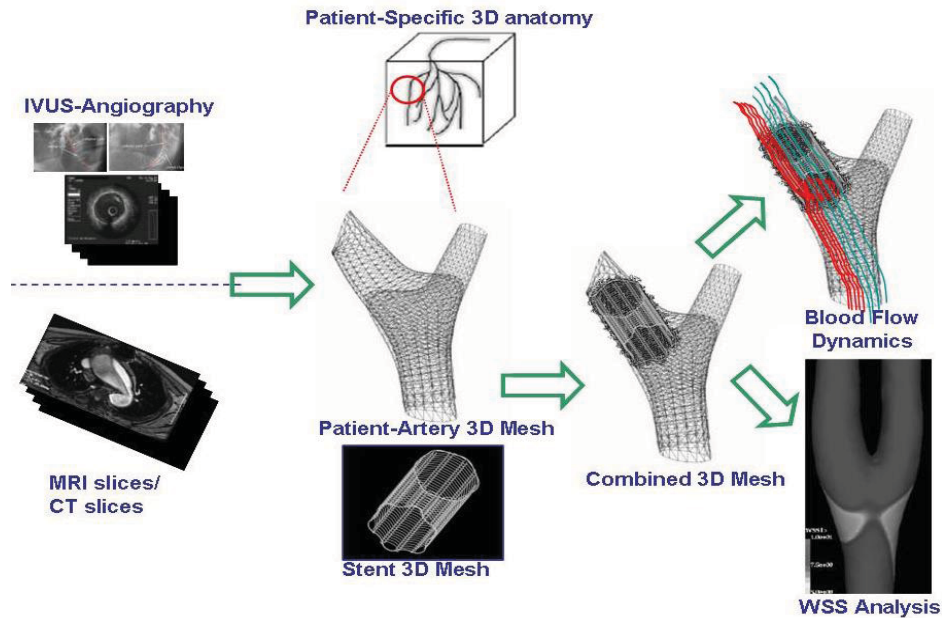


Figure 1: The conceptual Architecture of the patient specific 3D modeller (ARTool)

flow dynamics and (iii) plaque progression. For the 3D artery reconstruction, three approaches are used. First, 3-D coronary artery reconstruction is provided from IVUS and Angiography [9-13]. Two end-diastolic angiographic images are used to predict the catheter path. The artery path is approximated with cubic B-Splines and the catheter path is evolved by the intersection of two splines. IVUS frames are collected at the peak of R wave and by using deformable models and Neural Networks the lumen and outer vessel border are identified.

Second, carotid artery 3-D reconstruction is provided using MR images [14-16]. Edge detection techniques, along with active contour algorithms are used to extract the desired features and reconstruct the carotid 3D arterial model. Graphic API's are used in order to produce a smooth artery model. Finally, the patient-specific arterial tree can be performed by processing CT images [17-19]. Using similar techniques as above for processing CT slices, the tool can detect and reconstruct both coronary and carotid arterial trees. 3-D artery models are visualized with the tool and various measures can be provided to the medical experts. Blood flow dynamics is performed in both stented and unstented artery models, using finite element modelling for the fluid flow and mass transfer computations, even for deformable elastic artery walls and further modelling is considered taking into account genetic factors [20,21]. Regarding the plaque initiation and progression, two approaches are employed, the first using particle dynamic simulations and the second using partial and ordinary differential equations. An example of the procedure from 3D arterial tree reconstruction to wall shear stress distribution and to Low Density Lipoprotein (LDL) distribution is shown in Figs. 2, 3 and 4 respectively.

The ARTool software architecture is based on the Window Presentation Foundation technology, using the Windows Communication Foundation services approach (Fig. 5).

The software pattern used for this approach is the Model-View-Presenter Design Pattern. This Model-view-presenter (MVP) is a user interface design pattern engineered to facilitate automated unit testing and improve the separation of concerns in presentation logic.

The *model* is an interface defining the data to be displayed or otherwise acted upon in the user interface. The *view* is an interface that displays data (the model) and routes user commands (events) to the presenter to act upon that data. The *presenter* acts upon the model and the view.

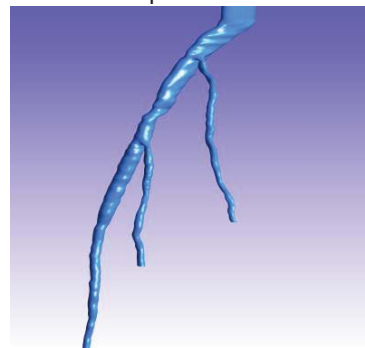


Figure 2: 3D reconstructed model of an arterial tree

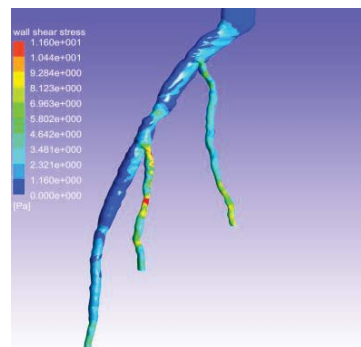


Figure 3: Wall Shear Stress Distribution in a 3D model

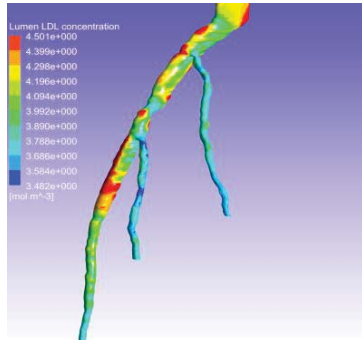


Figure 4: LDL distribution in a 3D model.

It retrieves data from repositories (the model), persists it, and formats it for display in the view. In terms of the ARTool software engineering platform, the above contain the following:

- The Model contains the data objects of the ARTool software.
- The View is a user control which contains windows components (like text boxes and buttons). The view raises events during interaction with the viewer.
- The Presenter deals with communication with the View and handles the events raised by the View

In terms of software engineering layers, in ARTool we have the following approach:

- The Data Storage Layer contains the ARTool database and the configuration files needed for the software operation.
- The Data Access Layer contains the implementation of the data retrieval and data storage methods from/to the database and files respectively.
- The Business Logic layer contains the implementation of the core methods as services and actual data context.
- The Graphical User Interface Layer contains all the graphical user controls (Views), which can be used in Presentation Layer.

In all of the above, the layers communicate using Services, which contain implementation of the business logic methods and algorithms using the Windows Communication Foundation principles and Interfaces, which deal with the communication of the Services. Fig. 6 presents an example of the interface that has been developed for the ARTool.

3. RESULTS

The tool can be used to visualize and predict the atherosclerotic plaque development. The accuracy of the underlying algorithms is estimated by evaluation which is based on medical images and experimental studies in animals and humans. More specifically, 3D reconstruction algorithms are validated using annotated images. The mean error of the lumen and media-adventitia area is $-0.63 \pm 8.71\%$ and $-2.09 \pm 8.61\%$, respectively in the IVUS and Angiography reconstruction. In the case of the carotid artery reconstruction using MRI the mean error is $-3.21 \pm 6.39\%$ and $1.92 \pm 5.88\%$ for the lumen and outer vessel wall, respectively. Finally,

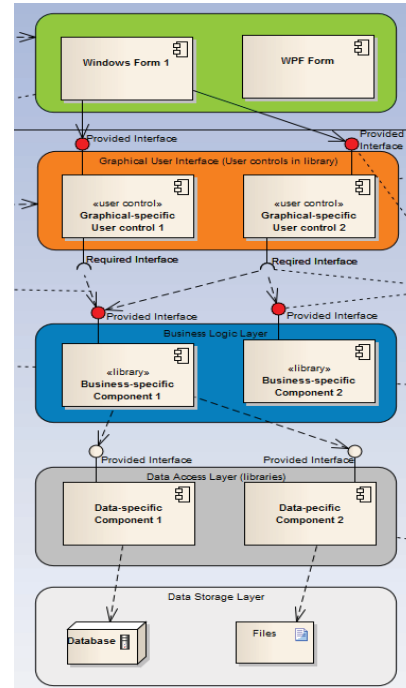


Figure 5: Architecture of the ARTool platform

reconstructed lumen area of arterial trees using CT images is 84.1% which means that the algorithm performs well compared to the state of the art. In addition to that, the expert has the capability to interact with the arterial segment, to pan or move into the artery and make easier a decision for the treatment.

Validation in blood flow modelling is achieved using Doppler or MRI data for coronary and carotid arteries, respectively. The mean error of the algorithm is about 4%.

4. DISCUSSION

The ARTool is a novel tool which provides 3D artery reconstruction, blood flow simulation and plaque formation modelling by processing various image modalities such as IVUS, Angiography, MRI and CT. All algorithms are incorporated into a friendly user interface. Coronary arteries are reconstructed fusing angiographic data which provide the information for coronary artery geometry, with IVUS data that reveal information about the distribution and constitution of the lumen and media-adventitia border. The user can inspect the segmentation of IVUS frames and the catheter path extraction process and visually assess the plaque burden in the final model.

Moreover, ARTool allows automated, fast and accurate 3D reconstruction of carotid arteries MRI data. Finally, the tool is able to reconstruct the coronary or carotid arterial tree using CT images. CT imaging appears a relatively new imaging modality with high sensitivity and specificity for the detection of luminal narrowing. ARTool can be used to overcome the increased time needed for the processing, as it includes an advanced methodology able to process the CT data and reconstruct the coronary tree.

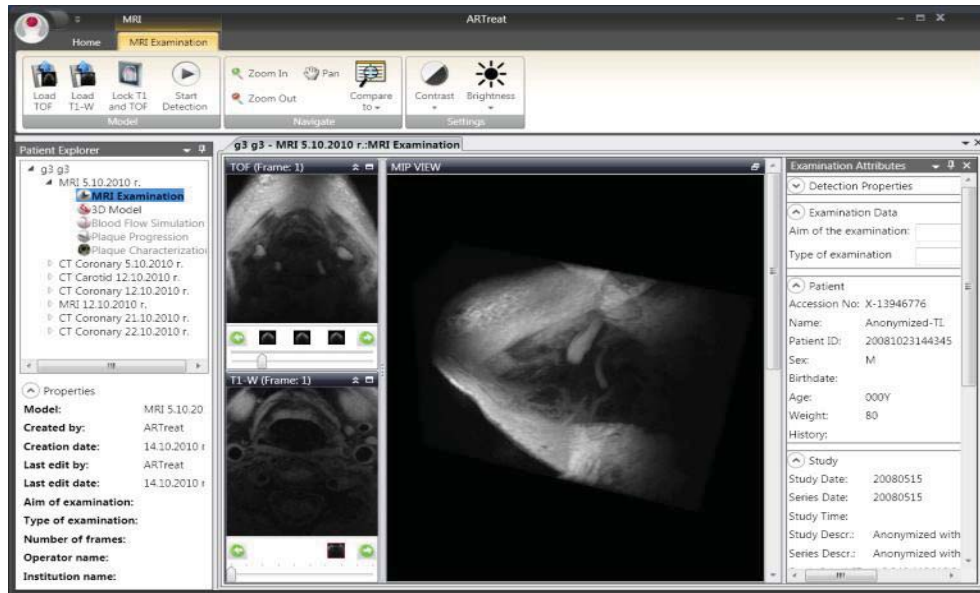


Figure 6: The interface of the ARTool platform

The quantitative analysis module that ARTool incorporates provides the user with important information such as the length of the arterial segment, the plaque volume, the minimum and the mean luminal cross sectional area, the length of the stenosis, and the maximum plaque burden. Finally, finite element method has been used to simulate blood flow and plaque development. Both methodologies provide patient-specific modelling facilitating the treatment decision. Furthermore, the methodologies are based on experimental results increasing the accuracy, while sensitivity analysis on a variety of parameters provides an estimation of the most accurate parameter values applied in the models.

REFERENCES

- [1] Bourantas, C., Kourtis, I., Plissiti, M., Fotiadis, D., Katsouras, C., Papafaklis, M., Michalis, L., "A Method for 3D reconstruction of coronary arteries using biplane angiography and intravascular ultrasound images," *Comp. Med. Imag. Gr.*, vol. 29, 2005, pp. 597-606.
- [2] Bourantas, C., Kalatzis, F., Papafaklis, M., Fotiadis, D., Tweddel, A., Kourtis, I., Katsouras, C., Michalis, L., "ANGIOCARE: An Automated System for Fast Three-Dimensional Coronary Reconstruction by Integrating Angiographic and Intracoronary Ultrasound Data," *Cath. and Cardio. Interv.*, vol. 72, 2008, pp. 166 – 175
- [3] Zifan, A., Liatsis, P., Kantartzis, P., Gavaises, M., Karcanias, N., Katritsis, D., "Automatic 3D Reconstruction of Coronary Artery Centerlines from Monoplane X-ray Angiogram Images," *International J. of Biolog. and Med. Sciences*, vol. 1, 2008, pp. 44 – 49
- [4] Auer, M., Stollberger, R., Regitnig, P., Ebner, F., Holzapfel, G.A., "3-D Reconstruction of Tissue Components for Atherosclerotic Human Arteries Using Ex Vivo High-Resolution MRI," *IEEE Transactions on Medical Imaging*, vol. 25, 2006, pp. 345 – 357
- [5] Steinman, D., Thomas, J., Ladak, H.M., Milner, J.S., Rutt, B.K., Spence, J.D., "Reconstruction of carotid bifurcation hemodynamics and wall thickness using computational fluid dynamics and MRI," *Magnetic Resonance in Medicine*, vol. 47, 2002, pp. 149 – 159
- [6] Čanić, S., Hartley, C., Rosenstrauch, D., Tambača, J., Guidoboni, G., Mikelić, A., "Blood Flow in Compliant Arteries: An Effective Viscoelastic Reduced Model, Numerics and Experimental Validation," *An. Biom. Eng.* vol. 34, 2006, pp. 575–592
- [7] Milner, J., Moore, J., Rutt, B., Steinman, D., "Hemodynamics of Human Carotid Artery Bifurcations: Computational Studies with Models Reconstructed from

- Magnetic Resonance Imaging of Normal Subjects," *J Vasc Surg.*, 1998, vol. 28, pp. 143-56
- [8] Holzapfel, G., Gasser, T., Ogden, R., "A New Constitutive Framework for Arterial Wall Mechanics and a Comparative Study of Material Models," *Journal of Elasticity*, vol. 61, 2000, pp. 1-48
- [9] Plissiti, M., Fotiadis, D., Michalis, L., Bozios, G., "An Automated Method for Lumen and Media-Adventitia Border Detection in a Sequence of IVUS Frames," *IEEE trans on Inf Tech. in Biomed.*, vol.8, 2004, pp. 131-141.
- [10] Papadogiorkaki, M., Chatzizisis, Y., "Automated IVUS Contour Detection using Intensity Features and Radial Basis Function Approximation," *IEEE International Symposium on Computer Based Medical Systems*, 2007.
- [11] Wahle, A., Prause, G., Dejong, S., Sonka, M., "Geometrically correct 3-D reconstruction of intravascular ultrasound images by fusion with biplane angiography – methods and validation," *IEEE Trans Med Imaging* vol. 18, 1999, pp. 686-98.
- [12] Laban, M., Oomen, J., Slager, C., Wentzel, J., Krams, R., Schuurbiens, J., "ANGUS: a New Approach to Three-Dimensional Reconstruction of Coronary Vessels by Combined Use of Angiography and Intravascular Ultrasound," *In: Proc. conf. CinC Vienna.*, 1995.
- [13] Slager, C., Wentzel, J., Schuurbiens, J., Oomen, J., Kloet, J., Krams, R., "True 3-Dimensional Reconstruction of Coronary Arteries in Patients by Fusion of Angiography and IVUS (ANGUS) and its Quantitative Validation" *Circulation*, vol. 102, 2000, pp. 511-6.
- [14] Xu, C., Prince, J., "Snakes, Shapes, and Gradient Vector Flow," *IEEE Trans on Image Proc.*, 7, 1998, pp. 359-369.
- [15] Canny, J., "A Computational Approach to Edge Detection," *IEEE Transactions on Pattern Analysis and Machine Intelligence*, vol. 8, 1986, pp. 679-698.
- [16] Barratt, D., Ariff, B., Humphries, K., Thom, S., Hughes, A., "Reconstruction and Quantification of the Carotid Artery Bifurcation from 3-D Ultrasound Images," *IEEE Trans. on Med. Imag.* vol. 23, 2004, pp. 567-583
- [17] Otsu, N., "A threshold selection method from gray level histograms," *IEEE Trans. Syst. Man Cyb.*, vol. 9, 1979, pp. 62–66
- [18] Kálmán, P., Erich, S., Emese, B., Attila, K., Csongor, H., Balázs, E., Klaus, H. "A Sequential 3D Thinning Algorithm and Its Medical Applications," *Lecture Notes in Computer Science.*, 2001, pp. 409-415
- [19] Dijkstra, E., "A note on two problems in connection with graphs". *In Num. Math.*, vol. 1, 1959, pp. 269–271
- [20] Feldman, C., Illegbusi, O., Hu, Z., Nesto, R., Waxman, S., Stone, P., "Determination of in vivo Velocity and Endothelial Shear Stress Patterns With Phasic Flow in Human Coronary Arteries: a Methodology to Predict Progression of Coronary Atherosclerosis," *Am Heart J.* vol. 143, 2002, pp. 931–9
- [21] Sakellarios, A., Fotiadis, D., Michalis, L., "Finite Element Modeling of LDL Transport in Carotid Artery Bifurcations." *EMBEK Conference*, Antwerp, 2008.

Welcome to IPSI BgD Conferences and Journals!

<http://www.internetconferences.net>

<http://www.internetjournals.net>

CIP – Katalogizacija u publikaciji

Narodna biblioteka Srbije, Beograd

ISSN 1820 – 4503

The IPSI BGD Transactions on Internet Research

COBISS.SR - ID 119128844

ISSN 1820-4511



9 771820 451006